

Emergence of dissipation and hysteresis from interactions among reversible, non-dissipative units: The case of fluid-fluid interfaces

Holtzman, R., Dentz, M., Moura, M., Chubynsky, M., Planet, R. & Ortín, J

Author post-print (accepted) deposited by Coventry University's Repository

Original citation & hyperlink:

Holtzman, R, Dentz, M, Moura, M, Chubynsky, M, Planet, R & Ortín, J 2024, 'Emergence of dissipation and hysteresis from interactions among reversible, non-dissipative units: The case of fluid-fluid interfaces', Physical Review Fluids, vol. 9, 064001 . <https://doi.org/10.1103/PhysRevFluids.9.064001>

DOI 10.1103/PhysRevFluids.9.064001

ESSN 2469-990X

Publisher: American Physical Society

Copyright © and Moral Rights are retained by the author(s) and/ or other copyright owners. A copy can be downloaded for personal non-commercial research or study, without prior permission or charge. This item cannot be reproduced or quoted extensively from without first obtaining permission in writing from the copyright holder(s). The content must not be changed in any way or sold commercially in any format or medium without the formal permission of the copyright holders.

This document is the author's post-print version, incorporating any revisions agreed during the peer-review process. Some differences between the published version and this version may remain and you are advised to consult the published version if you wish to cite from it.

1 **Emergence of dissipation and hysteresis from interactions among**
2 **reversible, non-dissipative units: The case of fluid-fluid interfaces**

3 Ran Holtzman,^{1,*} Marco Dentz,² Marcel Moura,³
4 Mykyta Chubynsky,¹ Ramon Planet,⁴ and Jordi Ortín⁴

5 ¹*Centre for Fluid and Complex Systems,*
6 *Coventry University, Coventry, United Kingdom*

7 ²*Institute of Environmental Assessment and Water Research (IDAEA),*
8 *Spanish National Research Council (CSIC), Barcelona, Spain*

9 ³*PoreLab, The Njord Centre, Department of Physics, University of Oslo, Oslo, Norway*

10 ⁴*Departament de Física de la Matèria Condensada,*
11 *Universitat de Barcelona, Barcelona, Spain,*

12 *and University of Barcelona Institute of Complex Systems, Barcelona, Spain*

Abstract

We examine the nonequilibrium nature of two-phase fluid displacements in a quasi-two-dimensional medium (a model open fracture), in the presence of localized constrictions (“defects”), from a theoretical and numerical standpoint. Our analysis predicts the capillary energy dissipated in abrupt interfacial displacements (jumps) across defects, and relates it to the corresponding hysteresis cycle, e.g. in pressure-saturation. We distinguish between “weak” (reversible interface displacement, exhibiting no hysteresis and dissipation) and “strong” (irreversible) defects. We expose the emergence of dissipation and irreversibility caused by spatial interactions, mediated by interfacial tension, among otherwise weak defects. We exemplify this cooperative behavior for a pair of weak defects and establish a critical separation distance, analytically and numerically, verified by a proof-of-concept experiment.

13 I. INTRODUCTION

14 Path-dependency (hysteresis) in pressure-saturation relationships during imbibition and
15 drainage in two-phase displacements in porous media occurs in wide variety of natural and
16 engineered processes, for instance soil moisture and geoenery [1, 2]. This hysteresis is
17 largely due to individual and cooperative capillary instabilities, known as Haines jumps [3],
18 which are inherently related to energy dissipation [4, 5]. The ubiquity of these phenomena in
19 various applications and the intriguing underlying physics motivated extensive experimental,
20 numerical and theoretical studies [5–12]. The intrinsic complexity of porous media and non-
21 local pore-scale interactions makes the quantitative understanding of the precise mechanisms
22 that lead to these phenomena a challenging task. Modeling approaches that account for the
23 metastability of two-fluid configurations and for hysteresis are often based on the aggregation
24 of individual hysteretic units (hysterons), in the so-called compartment models (e.g. [6, 7]).
25 Recently, based on quantitative insights from systematic studies in simplified model systems
26 that allow to isolate individual features causing hysteresis [13, 14], a novel approach that
27 does not rely on the concept of hysterons was suggested in [15].

28 However, the possibility that non-hysteretic units interact cooperatively to give rise to
29 hysteresis and dissipation remains unexplored, despite evidences from paradigmatic models

* ran.holtzman@coventry.ac.uk

30 of collective phenomena such as the Random Field Ising Model (RFIM) [16, 17]. Here
31 we address this open question by studying the passage of a two-phase interface through
32 localized perturbations in the capillary pressure, representing single topographic defects
33 (gap thickness constrictions) in a 2-D medium (Hele-Shaw cell).

34 Two-phase fluid flow in Hele-Shaw cells—quasi-two-dimensional setups formed by two
35 closely spaced parallel plates [18–20]—shares some salient features with two-phase flows
36 in porous and fractured media. In both, the bulk behavior of the flow of fluids in the
37 viscous (Stokes) regime can be described by Darcy’s law [21], and the stability of fluid-
38 fluid interfaces is controlled by viscosity and density contrasts between the fluids [22]. A
39 richer, more realistic model system is the “imperfect” Hele-Shaw cell, featuring gap-thickness
40 constrictions and expansions, in which the interfaces are subjected to capillary instabilities
41 akin to those observed in disordered media [13, 18]. Imperfect Hele-Shaw cells therefore
42 stand out as an ideal playground to study two-phase displacements in disordered media.

43 Using this model system, we study the notion of weak (reversible i.e. non-dissipative
44 and non-hysteretic) and strong (dissipative and hysteretic) defects. We first classify sin-
45 gle topographic defects as weak or strong, and quantify the associated energy dissipation
46 and hysteresis. We then demonstrate, analytically, numerically, and experimentally, the
47 emergence of dissipation and hysteresis due to spatial interactions (surface tension) among
48 individually weak defects. We show that a pair of weak defects that is non-dissipative if
49 separated far apart becomes strong (dissipative) when brought close enough together.

50 The paper is organized as follows. Section II provides background on quasistatic pressure-
51 driven displacements in imperfect Hele-Shaw cells, including the mathematical statements
52 of pressure equilibrium and energy dissipation. Section III presents the solution for the
53 interfacial configurations across single defects (capillary pressure distortions). We show the
54 functional form of the interfacial shapes, which also reveal subtle morphological differences
55 between imbibition and drainage, and distinct between weak (reversible, non-dissipative)
56 and strong (irreversible, dissipative) defects. Section IV uses the above to compute an en-
57 ergy balance from which we establish the energy dissipated during jumps. In Section V we
58 consider cooperative effects in the presence of multiple defects, with a nonintuitive result—
59 energy dissipation due to spatially-correlated interactions through interfacial tension for a
60 pair of weak defects brought sufficiently close together. A theoretical analysis provides a
61 critical value for the lateral separation between two weak defects that makes them collec-

62 tively dissipative. This prediction, derived in the limit of very narrow defects, is validated
63 against numerical simulations, and qualitatively verified experimentally. Finally, in Sec. VI
64 the original results of the work are briefly recalled and the main conclusions are drawn.
65 Specific details of the calculations, numerical simulations and experiments are provided in
66 the Appendices.

67 **II. BACKGROUND**

68 **A. Model system: Imperfect Hele-Shaw cell**

69 Quasistatic pressure-driven displacements in imperfect Hele-Shaw cells have shown
70 strongly nonlinear behavior and Haines jumps at pore and multipore scale, together with
71 lack of reversibility between opposite displacement directions (imbibition and drainage)
72 at continuum scale, hysteresis in the applied pressure vs wetting-phase saturation (PS)
73 trajectories, and the return-point memory (RPM) property of closed partial cycles that is
74 ubiquitous in porous media flows [14, 15, 23]. Below, we describe the theory allowing to
75 compute the interfacial configurations and energy dissipation for the general case of an im-
76 perfect Hele-Shaw cell with multiple defects (representing disordered media). In this paper
77 we apply these concepts to displacements through (i) isolated defects (local constrictions),
78 and (ii) a pair of defects, exposing their interaction.

79 **B. Establishing the equilibrium configurations**

80 The pressure balance of a two-phase interface invading an imperfect Hele-Shaw cell can
81 be derived in quasistatic conditions [14, 15]. Without loss of generality, we assume in the
82 following that the less wetting fluid is low-viscosity (e.g. air) and the more wetting fluid
83 is viscous (e.g. liquid such as silicone oil). We consider that (i) the gap thickness in the
84 cell changes in space (giving rise to an extended domain of connected constrictions and
85 expansions); (ii) the fluids are immiscible, and displacements are driven by the change of
86 the imposed pressure P at one end of the cell; and (iii) the cell is tilted in the direction that
87 prevents the formation of viscous fingers [22]. With these conditions, the linearized pressure

88 balance takes the form

$$\gamma \frac{d^2 h(x)}{dx^2} - \rho g_e h(x) + P + p_c[x, h(x)] = 0, \quad (1)$$

89 where $h(x)$ is the equilibrium interface position at x , γ the oil-air surface tension, ρ the oil
 90 density, g_e is the effective gravity (which in a physical implementation could be changed by
 91 tilting the cell, $g_e = g \sin \alpha$, where g is the gravitational acceleration and α the inclination an-
 92 gle from the horizontal). Here $p_c(x, y)$ is the perturbation in out-of-plane capillary pressure,
 93 determined by the variations in thickness (z). Here, the direction of the fluid advancement
 94 is parallel to the y -axis. For simplicity, we do not account for the minute variations in
 95 hydrostatic pressure of non-wetting fluid relative to the liquid pressure of the wetting fluid.
 96 Additionally, in our quasi-static model, the pressure changes associated with the viscosity of
 97 the two fluids are also neglected. The first and last terms in Eq. (1) account for the linearized
 98 in-plane component of the Young-Laplace pressure jump across the interface at each site x
 99 (for comparison with the exact nonlinear term see [23]), and the out-of-plane component
 100 arising from the presence of expansions and constrictions in the cell, respectively. The role
 101 of the two terms is different: the out-of-plane component is responsible for the interface
 102 deformation whereas the in-plane component is a restoring force resisting the deformation.
 103 In the quasistatic limit (zero driving rate) displacements are driven by minute changes of P ,
 104 separated by long time intervals required for reaching a new mechanical equilibrium $h(x)$.

105 The equilibrium configurations $h(x)$ could also be derived from minimizing the Hamilto-
 106 nian

$$\mathcal{H} = \int_{-\infty}^{\infty} dx \left(\frac{\gamma}{2} \left[\frac{dh(x)}{dx} \right]^2 + \int_0^{h(x)} dy [\rho g_e y - P - p_c(x, y)] \right), \quad (2)$$

107 and the pressure imbalance $p_e(x)$ experienced by the interface at each site x is given by
 108 $p_e(x) = -\delta\mathcal{H}/\delta h(x)$. The condition of mechanical equilibrium in Eq. (1) corresponds there-
 109 fore to setting $p_e(x) = 0$ [15]. In the framework of this model, PS trajectories are built
 110 from the sequence of equilibria. The passage from one equilibrium configuration to the next
 111 can be of two kinds. In the first, the system remains trapped in a *local* energy minimum,
 112 where the small change of external forcing P causes a correspondingly small evolution of the
 113 wetting-phase saturation S_w , resulting in a smooth PS trajectory. In the second, an abrupt
 114 change of state (S_w) takes place at the new value of P , in a Haines jump [3, 5]; this occurs

115 when the change of P suppresses the current local energy minimum, and the system is forced
 116 to abruptly jump to a new metastable equilibrium. Haines jumps are effectively instantane-
 117 ous in the time scale of change of the driving pressure, so that interfacial configurations
 118 experience irreversible changes at punctuated values of P .

119 Numerically, this dynamics can be simulated iteratively by *synchronous* updates of $h(x)$
 120 in all unstable sites by a small amount in the direction that reduces $|p_e(x)|$, stopping when all
 121 sites retain equilibrium (for details of the numerical procedure, see [15]). This deterministic
 122 rule is akin to the zero-temperature limit of the Glauber dynamics for RFIM [16, 24], which
 123 considers energy barriers between consecutive equilibria that are much larger than thermal
 124 fluctuations. The presence of the quenched disorder term $p_c[x, h(x)]$ in Eqs. (1) and (2)
 125 defines a rugged free energy landscape, so that for every applied pressure there are many
 126 different interfacial configurations $h(x)$ that are local minimizers of \mathcal{H} . The synchronous
 127 dynamics described above takes the current configuration to the closest available metastable
 128 minimum in a deterministic manner dictated by the quenched disorder. Ref. [15] proved that
 129 no parts of the interface recede under this dynamics, and a no-passing rule [25] is obeyed
 130 such that a configuration of larger (or equal) saturation compared to another will remain so
 131 under a monotonous evolution of the driving pressure. As a result, the original two-phase
 132 configuration is exactly recovered in any cyclic excursion of the driving pressure, a property
 133 known as RPM (return-point memory), ubiquitous to many athermal driven disordered
 134 systems [26–29].

135 C. Energy dissipated between equilibrium configurations

136 The amount of energy dissipated can be obtained from the change in interfacial energy
 137 due to fluid displacement and the mechanical work done by the applied pressure P . For a
 138 small interface displacement $\delta h(x)$ the dissipated energy is

$$d\Psi = dU - dW, \tag{3}$$

139 where dU is the change in the internal energy, and

$$dW = PdS = P \int_{-\infty}^{\infty} \delta h(x) dx \tag{4}$$

140 is the work. Here the notation $d\Box$ is used for infinitesimal changes of variables that are
 141 state functions (e.g. S), while $d\Box$ is for changes of variables that are not (e.g. W). In our
 142 2-D model, all energy units [Eq. (4) and throughout] are of energy per unit length, i.e. the
 143 out-of-plane thickness. U accounts for the capillary energy of the front deformation and for
 144 the gravitational potential energy of the oil phase (wetting fluid). We follow the convention
 145 that $d\Psi \leq 0$.

146 Noting that $\mathcal{H} = U - PS$, we get $\delta\mathcal{H} = d\Psi - S dP$. The fact that $\mathcal{H} = \mathcal{H}[h(x), P]$ and
 147 $p_e = -\delta\mathcal{H}/\delta h(x)$ allows writing

$$\delta\mathcal{H} = - \int_{-\infty}^{\infty} dx p_e(x) \delta h(x) - \int_{-\infty}^{\infty} dx \int_0^{h(x)} dy dP. \quad (5)$$

148 From this, as well as from Eq. (2) and the expression $\mathcal{H} = U - PS$, we can compute the
 149 internal energy as

$$U = \int_{-\infty}^{\infty} dx \left[\frac{\gamma}{2} \left(\frac{\partial h}{\partial x} \right)^2 + \int_0^h dy (\rho g_e y - p_c) \right] \quad (6)$$

150 Finally, the energy lost between two equilibrium states, $t - 1$ and t , is found by integrating
 151 Eq. (3), which gives [12]

$$\Psi^{t-1 \rightarrow t} = [U^t - U^{t-1}] - P^t [S_w^t - S_w^{t-1}]. \quad (7)$$

152 **D. Energy dissipated per incremental change in interface configurations**

153 Here, we present an alternative method for computing energy dissipation between consec-
 154 utive interfacial configurations. For continuous, reversible displacements (isons), where the
 155 system stays in one local minimum of \mathcal{H} , and a small change in P leads to a small change in
 156 $h(x)$, $p_e(x) = 0$ by definition. This reduces Eq. (5) to $\delta\mathcal{H} = - \int_{-\infty}^{\infty} dx \int_0^{h(x)} dy dP = -S dP$,
 157 which proves that $d\Psi = 0$, i.e., no dissipation. Since there are no energy losses in this case,
 158 $dW = dU$, and for a finite continuous displacement $W = \Delta U$, with ΔU computed from
 159 Eq. (6).

160 In irreversible displacements (rheons) P is constant ($dP = 0$) and $\delta\mathcal{H} = d\Psi$. This in turn
 161 provides the energy dissipated for each elementary step δh within a Haines jump, using Eq.

162 (5):

$$d\Psi = \delta\mathcal{H} = - \int_{-\infty}^{\infty} dx p_e(x) \delta h(x). \quad (8)$$

163 To obtain the total energy dissipated in a given jump between equilibrium states $t - 1$ and
 164 t , $\Psi^{t-1 \rightarrow t}$, one can integrate Eq. (8) over all the intermediate nonequilibrium steps k ,

$$\Psi^{t-1 \rightarrow t} = - \sum_k \int_{-\infty}^{\infty} dx p_e^k(x) \delta h^k(x). \quad (9)$$

165 Equations (8) and (9) present the energy dissipated as the sum of elementary products of
 166 unbalanced pressure $p_e(x)$ times the corresponding displacement $\delta h(x)$. This will be used
 167 below (Section III) to provide an explanation for a nonintuitive observation: asymmetry
 168 between energy dissipation in drainage and imbibition. Furthermore, Eqs. (8)–(9) show
 169 that the energy dissipation within avalanches does not have to be proportional to the corre-
 170 sponding change in saturation, as the values of $p_e(x)$ can be different from site to site. This
 171 non-proportionality between changes in saturation and dissipation was shown numerically
 172 in disordered media constructed from defects of various strengths [12]. A related finding was
 173 shown for quasistatically driven disordered ferromagnets [17]. An extreme example of this
 174 non-proportionality arises in the limit in which dissipation approaches zero even as the size
 175 of the interface jump remains finite, as we will see below.

176 III. INTERFACE CONFIGURATIONS: SINGLE DEFECT

177 In this Section, we formulate an analytical solution for the equilibrium interface configu-
 178 ration for a single defect. When an incompressible wetting fluid (e.g. oil) imbibes or drains
 179 quasistatically in a smooth Hele-Shaw cell with a narrow gap of fixed width, filled with
 180 inviscid, non-wetting fluid (e.g. air), the interface is morphologically stable and $h(x) = h_0$.
 181 Modulations of the out-of-plane capillary pressure, $p_c(x, y) = p_c^0 + \delta p_c(x, y)$, cause the inter-
 182 face to deform [14, 15, 30]. Expressing the modulation as $\delta p_c(x, y) = \delta p_c^* F(x, y)$, where δp_c^*
 183 is the maximum value and $F(x, y)$ is the “normalized modulation”, we can rewrite Eq. (1)
 184 as [14]

$$\gamma \frac{d^2 \eta(x)}{dx^2} - \rho g_e \eta(x) + \delta p_c^* F[x, \eta(x) + h_0] = 0, \quad (10)$$

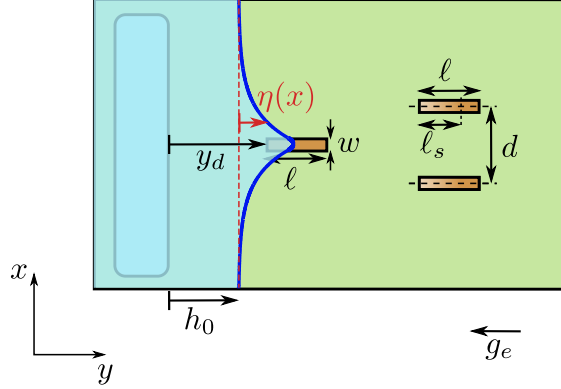


FIG. 1. Our 2-D model system representing an imperfect Hele-Shaw cell with local perturbations in thickness of width w and length ℓ (defects; in brown), which alter the out-of-plane capillary pressure p_c . Once the fluid-fluid interface (blue line) passes through a defect, the interface deforms by $\eta(x)$, measured relative to the flanks (which are at $y = h_0$) such that the interface height $h(x) = h_0 + \eta(x)$ is nonuniform. We consider both “mesa” defects (fixed p_c within the defect) and regular defects which include a sloping part of length ℓ_s (linear increase in p_c) and a plateau (fixed p_c). We also consider both a single, isolated defect, and a pair of interacting defects (separated by d); for simplicity, the interface, as well as its descriptors $[h_0, \eta(x)]$, and the defect position y_d are not shown for the defect pair.

185 where $\eta(x) = h(x) - h_0$ (Fig 1). Note that $h_0 = (P + p_c^0)/\rho g_e$. In the following we consider
 186 the case of $\delta p_c^* > 0$ ($\delta p_c^* < 0$ is analogous). We consider a defect with $F(x, y)$ nonzero within
 187 a rectangle $-w/2 < x < w/2$, $y_d < y < y_d + \ell$, where w is the width of the defect and ℓ its
 188 length. We do not set $y_d = 0$ to keep our formulation general such that it can be used for a
 189 disordered system with multiple defects.

190 The effective pressure field given by the left-hand side of Eq. (10) can be split into two
 191 parts: $p_e(x) = p_d(x) + \delta p_c^* F[x, \eta(x) + h_0]$, where p_d accounts for the restoring force of the
 192 line and it is linear in η [14]. We obtain the equilibrium states, $p_e = 0$, by equating

$$p_d(x) = -\delta p_c^* F[x, \eta(x) + h_0]. \quad (11)$$

193 Here, we find two different scenarios depending on the number of possible equilibrium con-
 194 figurations (roots) η_c that fulfill Eq. (11). If for all h_0 there is only one root, the defect does
 195 not lead to hysteresis or dissipation and is termed “weak”. In contrast, for an hysteretic
 196 and dissipative (“strong”) defect, for some interval of h_0 the solution gives three equilibrium
 197 points: two stable equilibrium configurations, with the largest and smallest η , while the
 198 intermediate one is unstable. We note that for complex p_c profiles it is possible to have

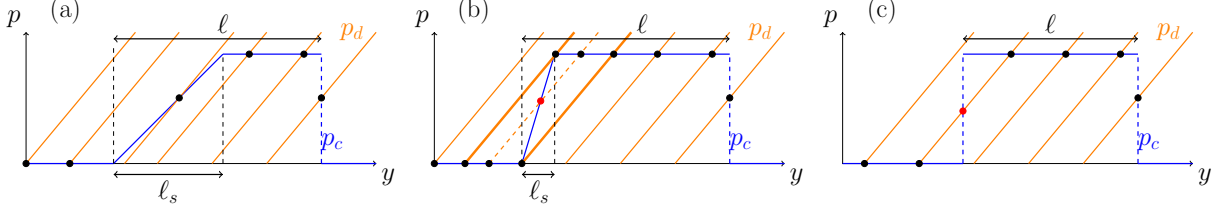


FIG. 2. Geometrical construction of the equilibrium positions of the interfaces in the presence of a localized defect: (a) weak; (b) strong; and (c) mesa. Blue lines correspond to the pressure field exerted by the defect. Orange lines correspond to the restoring force (pressure) of the interface, opposing the deformation. At equilibrium, $p_d = p_c$, and these states are presented as black dots for stable equilibrium. Red dots correspond to unstable states.

199 more than three roots; here we consider only linear variations in p_c .

200 Figure 2 shows visual representations of these different scenarios. These 1-D represen-
 201 tations are exact for infinitely wide defects (when there is no x dependence), and remain
 202 qualitatively valid for defects of arbitrary width. We refer to panels (a–b) as “regular” de-
 203 fects, where the change of p_c is continuous along the y axis. Panel (c) shows the special
 204 case of the “mesa” defect [13], where the modulation $F[x, \eta(x)]$ is a rectangular function in
 205 y , so that the change in p_c is discontinuous (non-regular). The 2-D interface shape when
 206 passing through a gap modulation can be derived by realizing that Eq. (10) can be written
 207 as $\delta p_c^* F[x, \eta(x) + h_0] = -\mathcal{L}\eta(x)$ with a linear differential operator \mathcal{L} . The interface shape
 208 $h(x)$ is obtained using the Green’s function formalism [14]

$$\eta(x) = \int_{-\infty}^{\infty} dx' G_0(x - x') \delta p_c^* F[x', h_0 + \eta(x')], \quad (12)$$

209 where $G_0(x)$ satisfies

$$\gamma \frac{d^2 G_0(x)}{dx^2} - \rho g_e G_0(x) = \delta(x), \quad (13)$$

210 It takes the form [14]

$$G_0(x) = \frac{\ell_c}{2\gamma} \exp(-|x|/\ell_c), \quad (14)$$

211 with $\ell_c = \sqrt{\gamma/(\rho g_e)}$.

212 **A. Interface configurations: Mesa defect**

213 For the special case of a mesa defect,

$$F(x, y) = \text{Rect}\left(\frac{x}{w}\right) \text{Rect}\left(\frac{y - (y_d + \ell/2)}{\ell}\right), \quad (15)$$

214 where $\text{Rect}(x)$ is the rectangular function $\text{Rect}(x) = H(x + 1/2) - H(x - 1/2)$, $H(x)$ is
 215 the Heaviside function, w is the width and ℓ the length of the defect. When passing such
 216 defects, the interface displacement is *always* hysteretic. The analytical solutions for the
 217 interface shape when passing through a mesa defect, derived in [15], are summarized below
 218 for completeness.

219 Assuming that for $|x| < w/2$, $h_0 + \eta$ is between y_d and $y_d + \ell$, the integral in Eq. (12) can
 220 be evaluated analytically, which gives

$$\eta(x) = \frac{\delta p_c^*}{\rho g_e} \begin{cases} \exp(-|x|/\ell_c) \sinh(w/2\ell_c), & |x| > w/2 \\ 1 - \exp(-w/2\ell_c) \cosh(x/\ell_c), & |x| \leq w/2 \end{cases} \quad (16)$$

221 The maximum deformation occurs at the defect centre $x = 0$, and equals

$$\eta_m = \frac{\delta p_c^*}{\rho g_e} [1 - \exp(-w/2\ell_c)]. \quad (17)$$

222 During imbibition, the interface remains flat until it contacts the defect, $h_0 = y_d$, at which
 223 point it deforms abruptly to a shape given by Eq. (16); here and elsewhere in this paper,
 224 we assume that the defect is sufficiently long to accommodate the deformed interface, i.e.,
 225 $\ell > \eta_m$. At the end of the defect, $y = y_d + \ell$, the interface gets pinned and deformation
 226 decreases continuously to zero (flat) by the time $h_0 = y_d + \ell$, at which point the interface
 227 exits the defect. During drainage, the initial part of the interface displacement is reversible
 228 (identical to that in imbibition), i.e. it gets pinned and deforms until $h_0 = (y_d + \ell) -$
 229 $(\delta p_c^*/\rho g_e) [1 - \exp(-w/2\ell_c)]$. However, when h_0 reaches y_d (the point of interface jump in
 230 imbibition), the trivial solution $\eta = 0$ appears as a metastable solution, but the interface
 231 remains deformed (thus, hysteresis is observed). The jump is delayed until h_0 is equal to

232 the external head h_c , given by

$$h_c = y_d - \frac{\delta p_c^*}{2\rho g_e} [1 - \exp(-w/\ell_c)] . \quad (18)$$

233 At that point the interface passes through the corners of the defect. For lower h_0 , the
 234 effective width w_e across which the defect is wet would have to be smaller than w , and the
 235 new equilibrium position would be

$$h_0 = y_d - \frac{\delta p_c^*}{2\rho g_e} [1 - \exp(-w_e/\ell_c)] > h_c. \quad (19)$$

236 However, this is not possible [15] and the nontrivial solution disappears.

237 Note that for a very wide defect ($w \gg \ell_c$), immediately before the jump during drainage
 238 the interface profile around $x = -w/2$ can be approximated as

$$h(x) = y_d + \frac{\delta p_c^*}{2\rho g_e} \begin{cases} \exp(\Delta x/\ell_c) - 1 , & \Delta x < 0, \\ 1 - \exp(-\Delta x/\ell_c) , & \Delta x > 0. \end{cases} \quad (20)$$

239 where $\Delta x = x + w/2$ and $|\Delta x| \ll w$. Thus, the solution is approximately symmetric
 240 with respect to the corner of the defect ($x = -w/2$, $y = y_d$) as the center of symmetry
 241 [$h(-w/2 + \Delta x) - y_d \approx -\{h(-w/2 - \Delta x) - y_d\}$]. Similarly for $x = w/2$ and the corresponding
 242 corner. We will compare this to the case of a wide regular defect with a slope below.

243 B. Interface configurations: Regular defect

244 We now consider a defect with a capillary pressure profile which varies in y ,

$$F(x, y) = a_1(x)c(y), \quad (21)$$

245 where

$$a_1(x) = \text{Rect} \left(\frac{x}{w} \right) \quad (22)$$

246 and

$$c(y) = \frac{1}{\ell_s} (y - y_d) \text{Rect} \left(\frac{y - y_d - \ell_s/2}{\ell_s} \right) + \text{Rect} \left(\frac{y - y_d - (\ell_s + \ell)/2}{\ell - \ell_s} \right). \quad (23)$$

247 The defect has width w and length ℓ , with the capillary pressure profile consisting of two
 248 parts: a slope (ramp) of length ℓ_s where p_c increases linearly in y and a plateau of fixed p_c
 249 (as in the mesa defect, cf. Fig. 1). In the ramp, the pressure slope is

$$\Pi = \frac{dp_c(0, y)}{dy} = \frac{\delta p_c^*}{\ell_s}. \quad (24)$$

250 The interface deformation is calculated by substituting Eq. (21) in the integral equation (12),

$$\eta(x) = \delta p_c^* \int_{-\infty}^{\infty} dx' G_0(x - x') a_1(x') c[h_0 + \eta(x')], \quad (25)$$

251 where the propagator $G_0(x)$ is given by Eq. (14).

252 In imbibition, prior to touching the defect, $h_0 < y_d$, the interface is undeformed, $\eta(x) = 0$.
 253 As the interface enters the defect, $h_0 > y_d$, as long as the interface deformation is small
 254 enough such that inside the defect it remains within the ramp, Eq. (25) becomes

$$\eta(x) = \Pi \int_{-\infty}^{\infty} dx' G_0(x - x') a_1(x') (h_0 - y_d) + \Pi \int_{-\infty}^{\infty} dx' G_0(x - x') a_1(x') \eta(x'). \quad (26)$$

255 We distinguish between two cases: the defect is *weak* if a solution of this equation exists, at
 256 least for small enough positive $h_0 - y_d$; it then changes continuously as h_0 increases. The
 257 defect is *strong* if there are no solutions for positive $h_0 - y_d$; in that case, upon entering the
 258 defect the interface experiences an abrupt jump that extends into the plateau.

259 To obtain a closed-form analytical solution, we consider below two limits: infinitely nar-
 260 row and infinitely wide defects. For these, we find the threshold between weak and strong,
 261 and the interface shapes before and after the jump in the strong regime. For the general
 262 case of a finite defect width, the threshold calculation is provided in Appendix A, and the
 263 numerical methods for establishing the interface shape are described in Appendix B.

264 The threshold between weak and strong defects in terms of the pressure slope, $\Pi_c^{(1)}$, is
 265 independent of ℓ_s given ℓ_c , w and γ . Dimensionality considerations provide

$$\Pi_c^{(1)} = \frac{\gamma}{\ell_c^2} f\left(\frac{w}{\ell_c}\right), \quad (27)$$

266 where f is a dimensionless function. Given $\Pi/\Pi_c^{(1)}$ and w/ℓ_c , the interface deformations
 267 before the jump in imbibition, η_{imb} , and after the jump in drainage, η_{dra} , are proportional
 268 to ℓ_s , thus,

$$\eta_{\text{imb}}(x) = \ell_s \phi_{\text{imb}} \left(\frac{x}{\ell_c}; \frac{\Pi}{\Pi_c^{(1)}}, \frac{w}{\ell_c} \right) \quad (28)$$

269 and

$$\eta_{\text{dra}}(x) = \ell_s \phi_{\text{dra}} \left(\frac{x}{\ell_c}; \frac{\Pi}{\Pi_c^{(1)}}, \frac{w}{\ell_c} \right), \quad (29)$$

270 where ϕ_{imb} and ϕ_{dra} are dimensionless functions.

271 1. Narrow defect limit ($w \ll \ell_c$)

272 Consider a narrow defect, $w \ll \ell_c$, located at $x = 0$. We note that $a_1(x) = w\delta_w(x)$ with
 273 $\delta_w(x) = w^{-1}\text{Rect}(x/w)$, where in the limit $w \rightarrow 0$, $\delta_w(x)$ approaches the Dirac delta $\delta(x)$.
 274 Introducing this approximation in Eq. (26), we obtain

$$\eta(x) = \Pi w(h_0 - y_d)G_0(x) + \Pi w\eta_0 G_0(x), \quad (30)$$

275 where $\eta_0 = \eta(0)$. For $x = 0$, this becomes

$$\eta_0 = \Pi w(h_0 - y_d)\beta_0 + \Pi w\eta_0\beta_0, \quad (31)$$

276 with $\beta_0 = G_0(0) = \ell_c/2\gamma$. This gives

$$\eta_0 = \frac{\Pi w\beta_0(h_0 - y_d)}{1 - \Pi w\beta_0}, \quad (32)$$

277 so that we obtain the following solution:

$$\eta(x) = G_0(x) \frac{\Pi w(h_0 - y_d)}{1 - \Pi w\beta_0}. \quad (33)$$

278 This is consistent with our assumption that the solution for the interface configuration
 279 crosses the defect within the ramp when $y_d < h_0 + \eta_0 < y_d + \ell_s$. This condition is satisfied

280 for sufficiently small and positive $h_0 - y_d$, when the denominator of Eq. (33) is positive, i.e.,

$$\Pi < \Pi_n^{(1)} = \frac{1}{w\beta_0} = \frac{2\gamma}{w\ell_c}. \quad (34)$$

281 In this case, the defect is weak. Here $\Pi_n^{(1)}$ is the narrow-defect approximation for the critical
 282 slope in a single defect, where the general threshold for a single defect, $\Pi_c^{(1)}$, is derived in
 283 Appendix A. Conversely, for $\Pi > \Pi_n^{(1)}$ there is no solution crossing the defect within the
 284 ramp for positive $h_0 - y_d$, indicating that the interface deforms abruptly beyond the sloping
 285 part, and the defect is strong. Note that a solution crossing the defect within the ramp
 286 does exist for strong defects when $h_0 - y_d$ is small enough and *negative*; this is the unstable
 287 solution marked by the red dot in Fig. 2(b).

288 For the case where the interface deforms beyond the ramp length and reaches the plateau
 289 region, Eq. (25) gives

$$\eta(x) = \delta p_c^* w G_0(x) = \delta p_c^* \frac{\ell_c w}{2\gamma} \exp(-|x|/\ell_c) = \frac{\Pi}{\Pi_n^{(1)}} \ell_s \exp(-|x|/\ell_c). \quad (35)$$

290 In cases where the defect width cannot be neglected, we make the assumption that the
 291 deformation is constant within the defect, providing

$$\eta(x) = \frac{\Pi}{\Pi_n^{(1)}} \ell_s \begin{cases} \exp[-(|x| - w/2)/\ell_c], & |x| > w/2, \\ 1, & |x| < w/2. \end{cases} \quad (36)$$

292 As expected, this coincides with the $w \ll \ell_c$ limit of the mesa defect case, Eq. (16). The
 293 deformation is independent of h_0 as long as the interface solution crosses the defect within
 294 the plateau. For a strong defect ($\Pi/\Pi_n^{(1)} > 1$), this occurs already for $h_0 = y_d$ [again,
 295 considering a sufficiently long defect, $\eta(0) = (\Pi/\Pi_n^{(1)})\ell_s < \ell$]. Thus, during imbibition, the
 296 interface jumps from

$$h = h_{\text{imb}}^- = y_d \quad (37)$$

297 to

$$h = h_{\text{imb}}^+ = y_d + \frac{\Pi}{\Pi_n^{(1)}} \ell_s \begin{cases} \exp[-(|x| - w/2)/\ell_c], & |x| > w/2, \\ 1, & |x| < w/2. \end{cases} \quad (38)$$

298 In drainage, in the beginning the interface displacement is identical to the mesa case, i.e.,

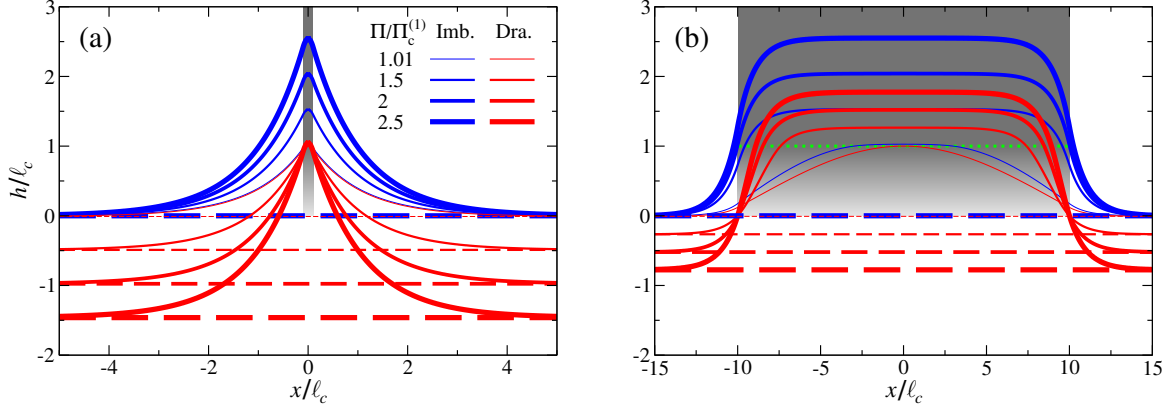


FIG. 3. Interface profiles before and after jumps for a narrow [$w/\ell_c = 0.2$; (a)] and a wide [$w/\ell_c = 20$; (b)] regular ramp defects, for different capillary pressure slopes. The ramp part of the defect is shown by a shading gradient, and the plateau part in uniform gray. The boundary between these two regions is at $h/\ell_c = 1$ and in panel (b) is marked with a green dotted line. Dashed and solid lines represent the undeformed (flat) and deformed configurations, i.e. before and after the jump in imbibition, and the opposite in drainage.

299 it pins at the edge of the defect, $y = y_d + \ell$, until the deformation reaches the value given
 300 by Eq. (36), and then moves continuously. The jump in drainage occurs when the interface
 301 reaches the boundary between the plateau and the ramp (rather than the end of the defect,
 302 $y = y_d$, in the mesa case), and the solution for the interface configuration, (36), meets the
 303 unstable branch and ceases to exist. At this point, $h_0 = y_d + \ell_s - \eta(0) = y_d - \ell_s(\Pi/\Pi_n^{(1)} - 1)$,
 304 and the jump occurs between

$$h_{\text{dra}}^- = \begin{cases} y_d - \ell_s \left\{ \frac{\Pi}{\Pi_n^{(1)}} [1 - \exp(-(|x| - w/2)/\ell_c)] - 1 \right\}, & |x| > w/2, \\ y_d + \ell_s, & |x| < w/2 \end{cases} \quad (39)$$

305 and

$$h_{\text{dra}}^+ = y_d - \ell_s(\Pi/\Pi_n^{(1)} - 1). \quad (40)$$

306 These interfacial jumps at various defect strengths, computed numerically for a suffi-
 307 ciently narrow defect $w/\ell_c = 0.2$ (Appendix B), are illustrated in Fig. 3a. As the transition
 308 between weak and strong is approached, $\Pi/\Pi_n^{(1)} \rightarrow 1+$, the difference between h_{imb}^+ and h_{dra}^-
 309 vanishes (barely noticeable for $\Pi/\Pi_n^{(1)} = 1.01$), although the jump remains finite (noting it
 310 can vanish for other defect profiles, not considered here).

312 In case of a very wide defect, the width of the Green's function G_0 [which is on the order
313 of ℓ_c ; see Eq. (14)] is much smaller than the width of the defect, and G_0 can be approximated
314 by a delta function,

$$G_0(x) \approx \frac{\ell_c^2}{\gamma} \delta(x), \quad (41)$$

315 such that Eq. (12) becomes

$$\eta(x) = \frac{\ell_c^2}{\gamma} \delta p_c^* F[x, h_0 + \eta(x)]. \quad (42)$$

316 This approximation is valid far from lateral boundaries of the defect. Outside the defect,
317 $\eta(x) = 0$. If the interface solution crosses the defect within the ramp, then inside the defect
318 we get from the above

$$\eta = \frac{\ell_c^2 \Pi}{\gamma} (h_0 + \eta - y_d), \quad (43)$$

319 and from this, or, equivalently from Eq. (26) with the same approximation for G_0 ,

$$\eta = \frac{(\ell_c^2 \Pi / \gamma)(h_0 - y_d)}{1 - \ell_c^2 \Pi / \gamma} = \frac{\Pi(h_0 - y_d)}{\rho g_e - \Pi}. \quad (44)$$

320 This solution crosses the defect within the ramp for small enough positive $h_0 - y_d$ if $\Pi <$
321 $\Pi_w^{(1)} = \rho g_e = \gamma / \ell_c^2$. In this case, the defect is weak. Here $\Pi_w^{(1)}$ is the wide-defect approxima-
322 tion for the general solution for the threshold for a single defect, $\Pi_c^{(1)}$, derived in Appendix A.
323 Otherwise (for $\Pi > \Pi_w^{(1)}$), during imbibition the interface jumps into the plateau upon touch-
324 ing it at y_d . In that case, the deformation of the interface part which is inside the defect not
325 too close to its edges is $\eta = \delta p_c^* / \rho g_e = \ell_s (\Pi / \Pi_w^{(1)})$, similar to that for the mesa defect [namely
326 Eq. (16) for $|x| < w/2$ except near the defect edges]. Thus, the interface configuration before
327 and after the jump is

$$h_{\text{imb}}^- = y_d \quad (45)$$

328 and

$$h_{\text{imb}}^+ = \begin{cases} y_d, & |x| > w/2, \\ y_d + \ell_s (\Pi / \Pi_w^{(1)}), & |x| < w/2. \end{cases} \quad (46)$$

329 An exception to the validity of this calculation is for $\Pi/\Pi_w^{(1)}$ just above and very close to
 330 1. In such case, Π may be above $\Pi_w^{(1)}$ yet below the exact threshold $\Pi_c^{(1)}$; even if not, the
 331 influence of the edges extends very far inside the defect (see Fig. 3b). For drainage (except
 332 for $\Pi/\Pi_c^{(1)} \approx 1$) immediately before the jump the interface passes very close to the corners
 333 of the defect at $y = y_d$; this is similar to the *mesa* but not to the *regular* narrow defect
 334 case. It can be shown then that the interface shape around the defect edge at $x = -w/2$
 335 still has a center of symmetry, but at height $y_d + \ell_s/2$, instead of in the corner of the defect.
 336 Mathematically, $h(x_0 + \Delta x) - y_d - \ell_s/2 \approx -[h(x_0 - \Delta x) - y_d - \ell_s/2]$ when $|\Delta x| \ll w$,
 337 where x_0 is such that $0 < x_0 + w/2 \ll w$, and analogously for x near $w/2$. The interfacial
 338 configurations before and after the jump in drainage are then

$$h_{\text{dra}}^- = \begin{cases} y_d - \ell_s \frac{\Pi/\Pi_w^{(1)} - 1}{2}, & |x| > w/2, \\ y_d + \ell_s \frac{\Pi/\Pi_w^{(1)} + 1}{2}, & |x| < w/2. \end{cases} \quad (47)$$

339 and

$$h_{\text{dra}}^+ = y_d - \ell_s \frac{\Pi/\Pi_w^{(1)} - 1}{2}. \quad (48)$$

340 These analytical expressions are confirmed by the numerical computations (Appendix B),
 341 see Fig. 3b.

342 IV. ENERGY BALANCE: DISSIPATION DURING JUMPS

343 We begin by considering a closed imbibition-drainage cycle for a strong defect. The first
 344 dissipation event occurs when the interface enters the defect in imbibition. The external
 345 pressure is $\rho g_e h_0 = \rho g_e h_{\text{imb}}^- = \rho g_e y_d$, and the work is $W_{\text{imb}} = \rho g_e y_d \int_{-\infty}^{\infty} dx \eta_{\text{imb}}(x)$; here we
 346 used the fact that the deformation after the jump, $\eta_{\text{imb}}(x)$, equals $h_{\text{imb}}^+ - h_{\text{imb}}^-$. The internal
 347 energy change during this deformation is

$$\begin{aligned} \Delta U_{\text{imb}} &= U\{h_{\text{imb}}^+\} - U\{h_{\text{imb}}^-\} \\ &= \int_{-\infty}^{\infty} dx \left[\frac{\gamma}{2} \left(\frac{d\eta_{\text{imb}}}{dx} \right)^2 + \frac{\rho g_e}{2} (\eta_{\text{imb}}^2 + 2y_d \eta_{\text{imb}}) - \delta p_c^* \int_{y_d}^{y_d + \eta_{\text{imb}}} dy F(x, y) \right], \end{aligned} \quad (49)$$

348 where $U\{h\}$ denotes the functional dependence of the internal energy on the interface con-
 349 figuration. Thus, we obtain for the dissipated energy

$$\Psi_{\text{imb}} = \Delta U_{\text{imb}} - W_{\text{imb}} = \int_{-\infty}^{\infty} dx \left[\frac{\gamma}{2} \left(\frac{d\eta_{\text{imb}}}{dx} \right)^2 + \frac{\rho g_e}{2} \eta_{\text{imb}}^2 - \delta p_c^* \int_{y_d}^{y_d + \eta_{\text{imb}}} dy F(x, y) \right]. \quad (50)$$

350 The second dissipation event occurs when the interface leaves the defect in drainage. The
 351 work done on the interface is $W_{\text{dra}} = -\rho g_e h_{\text{dra}}^+ \int_{-\infty}^{\infty} dx \eta_{\text{dra}}(x)$, where the deformation of the
 352 interface before the jump, $\eta_{\text{dra}}(x) = h_{\text{dra}}^- - h_{\text{dra}}^+$. The change of internal energy is

$$\begin{aligned} \Delta U_{\text{dra}} &= U\{h_{\text{dra}}^+\} - U\{h_{\text{dra}}^-\} \\ &= - \int_{-\infty}^{\infty} dx \left[\frac{\gamma}{2} \left(\frac{d\eta_{\text{dra}}(x)}{dx} \right)^2 + \frac{\rho g_e}{2} (\eta_{\text{dra}}^2 + 2h_{\text{dra}}^+ \eta_{\text{dra}}) - \delta p_c^* \int_{h_{\text{dra}}^+}^{h_{\text{dra}}^+ + \eta_{\text{dra}}} dy F(x, y) \right]. \end{aligned} \quad (51)$$

353 This provides the following dissipated energy:

$$\Psi_{\text{dra}} = \Delta U_{\text{dra}} - W_{\text{dra}} = - \int_{-\infty}^{\infty} dx \left[\frac{\gamma}{2} \left(\frac{d\eta_{\text{dra}}(x)}{dx} \right)^2 + \frac{\rho g_e}{2} \eta_{\text{dra}}^2 - \delta p_c^* \int_{h_{\text{dra}}^+}^{h_{\text{dra}}^+ + \eta_{\text{dra}}} dy F(x, y) \right]. \quad (52)$$

354 A. Energy Dissipation: Mesa defect

355 For imbibition in a mesa defect, in the rightmost term in Eq. (50)

$$\int_{y_d}^{y_d + \eta_{\text{imb}}} dy F(x, y) = \text{Rect}(x/w) \eta_{\text{imb}}(x), \quad (53)$$

356 which, together with the fact that η_{imb} equals η from Eq. (16), allows us to calculate the
 357 integral in Eq. (50), giving

$$\Psi_{\text{imb}} = - \frac{1}{2} \frac{\delta p_c^{*2} \ell_c}{\rho g_e} \left[\frac{w}{\ell_c} + \exp(-w/\ell_c) - 1 \right]. \quad (54)$$

358 Similarly, for drainage we substitute in Eq. (52) h_{dra}^+ for h_c from Eq. (18), to obtain

$$\int_{h_{\text{dra}}^+}^{h_{\text{dra}}^+ + \eta_{\text{dra}}} dy F(x, y) = \text{Rect}(x/w) [\eta_{\text{dra}}(x) + h_c - y_d]. \quad (55)$$

359 Using η from Eq. (16) for η_{dra} in Eq. (52) gives

$$\Psi_{\text{dra}} = -\frac{1}{2} \frac{\delta p_c^{*2} \ell_c}{\rho g_e} \left[1 - \left(1 + \frac{w}{\ell_c} \right) \exp(-w/\ell_c) \right]. \quad (56)$$

360 The total dissipated energy for a closed hysteresis cycle, $\Psi_{\text{tot}} = \Psi_{\text{imb}} + \Psi_{\text{dra}}$, is given by

$$\Psi_{\text{tot}} = -\frac{w \delta p_c^{*2}}{2 \rho g_e} [1 - \exp(-w/\ell_c)]. \quad (57)$$

361 In the narrow defect limit, $w \ll \ell_c$, we get

$$\Psi_{\text{imb}} \approx \Psi_{\text{dra}} \approx -\frac{1}{4} \frac{\delta p_c^{*2} w^2}{\rho g_e \ell_c}. \quad (58)$$

362 This dependence on system parameters is expected when analyzing the terms in Eqs. (54)
 363 and (56) separately, as they are all of the same order of magnitude. In particular, the
 364 dependence on the defect width w is quadratic, as $\eta_m \sim w$ [fixing all other parameters in
 365 Eq. (58)] and the width of the region where $\eta \approx \eta_m$ is w -independent.

366 For the wide-defect limit, $w \gg \ell_c$, dissipation in imbibition reduces to

$$\Psi_{\text{imb}} \approx -\frac{1}{2} \frac{\delta p_c^{*2} w}{\rho g_e}. \quad (59)$$

367 Here, the dependence on w is linear and matches those of the second and third terms in
 368 Eq. (54); this is because η_{imb} in the wide-defect limit is (i) approximately constant in the
 369 region of width $\approx w$, and (ii) that constant is w -independent [fixing all other parameters in
 370 Eq. (59)]. The first term in Eq. (54) is negligible (as the integrand peaks near the edges of
 371 the defect in regions of width $\sim \ell_c \ll w$).

372 For drainage in the wide-defect limit, the dissipation is

$$\Psi_{\text{dra}} \approx -\frac{1}{2} \frac{\delta p_c^{*2} \ell_c}{\rho g_e}. \quad (60)$$

373 This is width-independent, and considerably smaller than in imbibition (Ψ_{imb}), suggesting
 374 that the second and third terms approximately cancel out. Thus, in the wide defect limit,
 375 dissipation can be thought of as coming from the edges of the defect, rather than its whole
 376 width. This can also be seen by examining the out-of-equilibrium pressure (p_e) during
 377 a jump, which is used in Eqs. (8)–(9) to compute the dissipation as a force-displacement
 378 product; this is illustrated in Video S1 in [Supplementary Information \(SI\)](#). The imbalance at
 379 the edges in drainage implies that it is the source for a appreciable portion of the dissipation.
 380 We note that as the example in Video S1 is for a moderately-wide defect (not the wide-defect
 381 limit), a substantial part of the dissipation is associated with the motion of the central parts
 382 of the interface.

383 B. Energy Dissipation: Regular defect

384 For regular defects, the last term in the dissipation calculations, Eqs. (50) and (52),
 385 becomes more complicated, because the defect consists of two parts. With $F(x, y)$ given by
 386 Eq. (21), this term is

$$\int_{y_d}^{y_d + \eta_{\text{imb}}} dy F(x, y) = \text{Rect}(x/w) \begin{cases} \eta_{\text{imb}}^2 / (2\ell_s), & \eta_{\text{imb}} < \ell_s, \\ \eta_{\text{imb}} - \ell_s/2, & \eta_{\text{imb}} > \ell_s, \end{cases} \quad (61)$$

387 for imbibition, and

$$\int_{h_{\text{dra}}^+}^{h_{\text{dra}}^+ + \eta_{\text{dra}}} dy F(x, y) = \text{Rect}(x/w) \begin{cases} (\eta_{\text{dra}} + h_{\text{dra}}^+ - y_d)^2 / (2\ell_s), & \eta_{\text{dra}} < \ell_s + y_d - h_{\text{dra}}^+, \\ \eta_{\text{dra}} + h_{\text{dra}}^+ - y_d - \ell_s/2, & \eta_{\text{dra}} > \ell_s + y_d - h_{\text{dra}}^+ \end{cases} \quad (62)$$

388 for drainage.

389 Calculating dissipation analytically (or even finding the expression for η) for regular
 390 defects of an arbitrary width and slope is considerably more difficult than for mesa defects.
 391 This is because the solution for the interface can be in both the ramp and the plateau parts
 392 of the defect, requiring matching between all the different parts of the interface. Numerical
 393 results for η_{imb} and η_{dra} can be obtained as described in Appendix B, followed by numerical
 394 integration to obtain Ψ_{imb} and Ψ_{dra} . Nonetheless, analytical results can be obtained for

395 specific cases. First, as there is no dissipation for weak defects, the dissipated energy for both
 396 imbibition and drainage vanishes as the defect strength approaches the limit $\Pi/\Pi_c^{(1)} \rightarrow 1+$.
 397 On the other hand, for $\Pi/\Pi_c^{(1)} \gg 1$, the interface solution crosses the defect entirely within
 398 the plateau region, and therefore η_{imb} and η_{dra} equal those for a mesa defect with the same
 399 w and δp_c^* . Therefore, the first two terms in Eqs. (50) and (52) are identical for mesa and
 400 regular defects. If the interface jumps far into the plateau region, the third term resembles
 401 that in the mesa case (e.g., for imbibition $\eta_{\text{imb}} - \ell_s/2 \approx \eta_{\text{imb}}$); if it is not (as is the case for
 402 narrow defects in drainage, see Fig. 3a), the term is negligible. Therefore, the dissipation
 403 for $\Pi/\Pi_c^{(1)} \gg 1$ is approximately equal to that in a mesa defect (with the same w and δp_c^*),

$$\Psi_{\text{imb}} \approx -\frac{1}{2} \frac{\delta p_c^* \ell_c}{\rho g_e} \psi_{\text{imb}} = -\frac{\ell_s^2 \ell_c^3 \Pi^2}{2\gamma} \psi_{\text{imb}} \quad (63)$$

404 and

$$\Psi_{\text{dra}} \approx -\frac{\ell_s^2 \ell_c^3 \Pi^2}{2\gamma} \psi_{\text{dra}}. \quad (64)$$

405 Here,

$$\psi_{\text{imb}} = \frac{w}{\ell_c} + \exp(-w/\ell_c) - 1 \quad (65)$$

406 and

$$\psi_{\text{dra}} = 1 - \left(1 + \frac{w}{\ell_c}\right) \exp(-w/\ell_c). \quad (66)$$

407 Both the approach to zero dissipation as $\Pi \rightarrow \Pi_c^{(1)}$, and the approach to the mesa results
 408 for $\Pi/\Pi_c^{(1)} \gg 1$, are confirmed by Fig. 4, where numerical computations for a regular defect
 409 of an intermediate width ($w/\ell_c = 2$) are compared to analytical mesa results.

410 Similarly, it is easy to calculate the dissipation for a regular defect with an arbitrary
 411 slope Π , in the narrow defect limit ($w \ll \ell_c$). The dissipation, that turns out to be equal
 412 in imbibition and drainage, is obtained using Eqs. (37)–(40) for the interface shapes [h_{imb}^- ,
 413 h_{imb}^+ , h_{dra}^- and h_{dra}^+] in Eqs. (50), (52), (61) and (62), as well as the expression for $\Pi_n^{(1)}$ given
 414 by Eq. (34):

$$\Psi_{\text{imb}} = \Psi_{\text{dra}} = -\frac{w \ell_s^2}{2} \Pi \left(\frac{\Pi}{\Pi_n^{(1)}} - 1 \right) = -\frac{\ell_s^2 \ell_c^3}{4\gamma} \Pi (\Pi - \Pi_n^{(1)}) \left(\frac{w}{\ell_c} \right)^2. \quad (67)$$

415 This equals the dissipation for the mesa defect in Eqs. (63)–(64) when both (i) $w \ll \ell_c$, in
 416 which case we can approximate the expressions in Eqs. (65)–(66) by $(1/2)(w/\ell_c)^2$; and (ii)

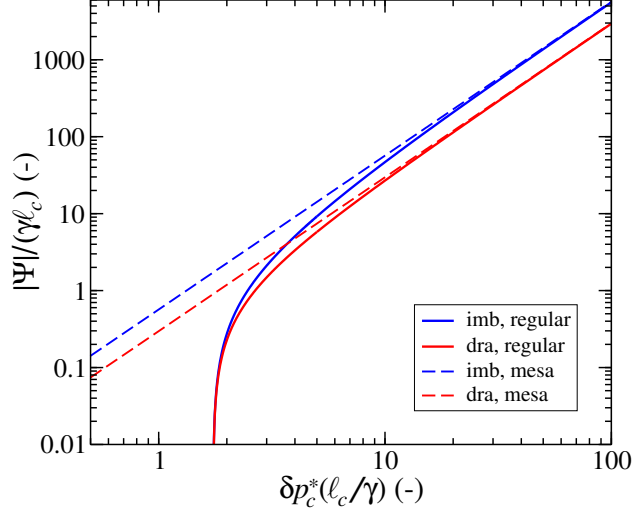


FIG. 4. Dimensionless dissipated energy against dimensionless capillary pressure perturbation for mesa and regular defects with $w/\ell_c = 2$ ($\ell_s/\ell_c = 1$ for regular defects). For very strong defects (large δp_c^*), the results for mesa and regular defects converge. The difference between imbibition and drainage, which is significant for mesa defects as well as for very strong regular defects, vanishes as δp_c approaches the threshold between weak and strong.

417 $\Pi \gg \Pi_n^{(1)}$, when $\Pi(\Pi - \Pi_n^{(1)}) \approx \Pi^2$ in Eq. (67).

418 It is useful to consider the following dimensionless quantity,

$$\psi = -\frac{\Psi}{\ell_s^2 \ell_c^3 \Pi(\Pi - \Pi_c^{(1)})/(2\gamma)}. \quad (68)$$

419 For arbitrary defect widths and slopes, Eqs. (27)–(29) predict that ψ depends only on the
 420 dimensionless parameters w/ℓ_c and $\Pi/\Pi_c^{(1)}$. According to Eq. (67), for narrow defects it is
 421 expected to depend only on w/ℓ_c (and be identical for imbibition and drainage), while for
 422 an arbitrary width w it should approach the expressions in Eqs. (65)–(66) as $\Pi/\Pi_c^{(1)} \rightarrow \infty$.
 423 This is demonstrated by plotting the dissipation for various defect widths w and $\Pi/\Pi_c^{(1)}$
 424 (Fig. 5). Figure 5 also shows that as $\Pi/\Pi_c^{(1)} \rightarrow 1$, ψ approaches a finite value, and therefore
 425 the dissipation is linear in $\Pi - \Pi_c^{(1)}$ just above the threshold; this was shown in Eq. (67)
 426 for narrow defects, here confirmed for an arbitrary width. This linear dependence is a
 427 consequence of the finite interfacial jump; a faster approach to zero is expected when this is
 428 not so. Moreover, the limits for ψ as $\Pi/\Pi_c^{(1)} \rightarrow 1$ are the same for imbibition and drainage,
 429 see also Fig. 4. Therefore, the dissipation for imbibition and drainage is similar for narrow
 430 defects (regardless of strength Π) and for arbitrary widths when $\Pi - \Pi_c^{(1)} \ll \Pi_c^{(1)}$.

431 The dependence of dissipation on the defect width for a regular defect is similar to that

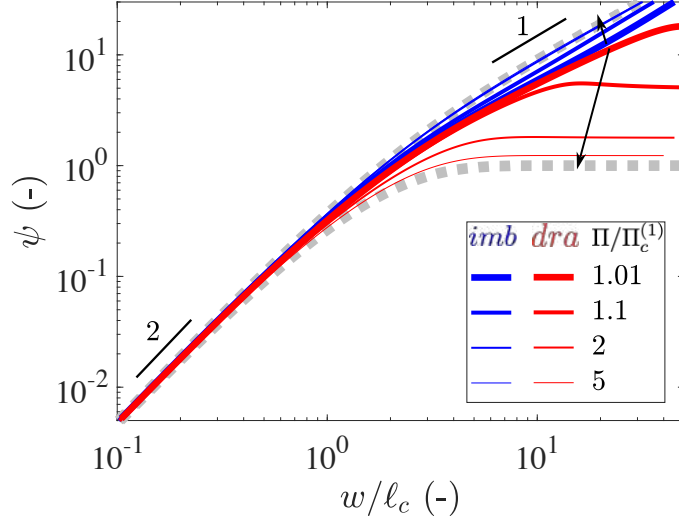


FIG. 5. Rescaled dissipated energy ψ [Eq. (68)] in imbibition (blue) and drainage (red) for various values of $\Pi/\Pi_c^{(1)}$ (a single regular defect). For narrow defects ($w/\ell_g \ll 1$), the imbibition and drainage curves collapse (independently of $\Pi/\Pi_c^{(1)}$), with $\psi \propto w^2$. For arbitrary widths, for small slopes i.e. $\Pi/\Pi_c^{(1)} \rightarrow 1$, imbibition and drainage approach the same limit, whereas as the slope increases (“stronger” defect; black arrows), $\Pi/\Pi_c^{(1)} \rightarrow \infty$, the dissipation approaches the bounding values of the dissipation in a mesa defect (dashed gray), given by the expressions in Eqs. (65)–(66). For imbibition at very wide defects, dissipation scales with the width, $\psi \propto w^1$.

432 for a mesa defect for fixed $\Pi \gg \Pi_c^{(1)}$. This can be explained by considerations similar to
 433 those we used for the mesa defects. For narrow defects, all the terms in Eqs. (50) and (52)
 434 are of the same order of magnitude and $\propto w^2$. For wide defects, the second and third terms
 435 are $\propto w$, giving rise to that dependence of Ψ on w in imbibition, but they cancel out for
 436 drainage resulting in w -independent dissipation. However, in contrast to mesa defects, for
 437 regular defects dissipation also vanishes as $\Pi \rightarrow \Pi_c^{(1)}$, i.e. the terms that are of the same
 438 order of magnitude must cancel out. This is easy to confirm for imbibition in wide defects,
 439 where the first term is negligible and the last two terms in the integrand are constant within
 440 the defect not too close to its edges. The sum of these terms is

$$\frac{\rho g_e}{2} \eta_{\text{imb}}^2 - \delta p_c^* \int_{y_d}^{y_d + \eta_{\text{imb}}} dy F(x, y) = \begin{cases} (1/2)(\rho g_e - \Pi) \eta_{\text{imb}}^2, & \eta_{\text{imb}} < \ell_s, \\ (1/2)(\rho g_e - \Pi) \eta_{\text{imb}}^2 + (\Pi/2)(\eta_{\text{imb}} - \ell_s)^2, & \eta_{\text{imb}} > \ell_s, \end{cases} \quad (69)$$

441 where we have used Eq. (61). This has the incorrect (positive) sign for any $\eta_{\text{imb}} > 0$ when

442 $\Pi < \Pi_w^{(1)} = \rho g_e$, thus, there are no nonzero solutions for η_{imb} , i.e., no stable deformed
 443 configurations, and the defect is weak. For a strong defect [$\Pi > \Pi_w^{(1)}$] and $\eta_{\text{imb}} = \ell_s(\Pi/\Pi_w^{(1)})$
 444 [see Eqs. (45)–(46)], this sum is negative and approaches zero when $\Pi \rightarrow \Pi_w^{(1)}$, as expected.
 445 We can also verify that the last two terms in the expression for drainage cancel out for *any*
 446 $\Pi > \Pi_w^{(1)}$. For $\eta > \ell_s + y_d - h_{\text{dra}}^+$ the sum of these terms becomes

$$\frac{\rho g_e}{2} \eta_{\text{imb}}^2 - \delta p_c^* \int_{h_{\text{dra}}^+}^{h_{\text{dra}}^+ + \eta_{\text{dra}}} dy F(x, y) = \frac{\Pi_w^{(1)}}{2} \eta_{\text{dra}}^2 - \Pi \ell_s (\eta_{\text{dra}} + h_{\text{dra}}^+ - y_d - \ell_s/2), \quad (70)$$

447 where we used Eq. (62). Using Eq. (47) for $h_{\text{dra}}^- = \eta_{\text{dra}} + h_{\text{dra}}^+$ and Eq. (48) for h_{dra}^+ , we see
 448 that the sum vanishes for all Π values.

449 V. COOPERATIVE ORIGIN OF HYSTERESIS AND DISSIPATION

450 A single mesa defect is strong, with interface displacement (e.g. PS trajectory) which is
 451 hysteretic and irreversible (dissipative). A disordered medium composed of multiple mesa
 452 defects, is also hysteretic and dissipative [12]. From this, one might naively conclude that
 453 the overall hysteretic response is simply the sum of the response of basic hysteretic entities
 454 (here, “defects”). This conforms with the conventional thinking behind compartment models
 455 such as Leverett and Preisach (where basic hysteretic entities are called “hysterons”) [26].
 456 Following the same logic, one would expect that a medium composed of multiple weak
 457 defects—each of which is non-hysteretic, reversible and non-dissipative—will also be non-
 458 hysteretic and reversible. To examine this, we consider a simple system composed of two
 459 identical regular, weak defects of width w at a distance d apart (measured between their
 460 centers, with $d \geq w$), positioned at $y = y_d$ (Fig 1). Similarly to the single defects considered
 461 in Sections. III and IV, each defect has a capillary pressure profile which is linearly increasing
 462 in y over a distance ℓ_s , after which it remains constant (plateau), with the total defect length
 463 ℓ . For each system with a given interdefect distance d , we compute the energy dissipated in
 464 imbibition and drainage, analytically and numerically, as described below.

465 **A. Interactions between a pair of weak defects: Analytical evaluation**

466 The local pressure balance in Eq. (10) is general, and thus it can be used for any number
 467 of defects, regular or irregular. For the pair of weak defects considered here, we write the
 468 capillary pressure profile as

$$F(x, y) = a_2(x)c(y), \quad (71)$$

469 where $c(y)$ has the same form as in the single regular defect case [Eq. (23)], with the term
 470 $a_1(x)$ [Eq. (22)] replaced here with $a_2(x)$ consisting of two rectangular functions,

$$a_2(x) = \text{Rect}\left(\frac{x + d/2}{w}\right) + \text{Rect}\left(\frac{x - d/2}{w}\right) = w [\delta_w(x + d/2) + \delta_w(x - d/2)], \quad (72)$$

471 where we use $\delta_w(x)$ introduced in Section III B 1. Note that for $d = w$, the two-defect system
 472 reduces to a single defect of width $2w$.

473 Consider the case when the defects are narrow ($w/\ell_c \ll 1$), so that we can replace
 474 $\delta_w(x) \rightarrow \delta(x)$. Using the resulting approximation of $a_2(x)$ in (26) (substituting a_2 for a_1),
 475 under the assumption that the interface solution crosses the defects within the ramps, the
 476 deformation is

$$\eta(x) = \Pi w [G_0(x + d/2) + G_0(x - d/2)] [(h_0 - y_d) + \eta_1], \quad (73)$$

477 where we set $\eta_1 = \eta(-d/2) = \eta(d/2)$ by using the symmetry of the domain. Imposing
 478 $x = d/2$ in (73), we obtain

$$\eta_1 = \frac{\Pi w \beta_1 (h_0 - y_d)}{1 - \Pi w \beta_1} \quad \text{with} \quad \beta_1 = G_0(d) + G_0(0) \quad (74)$$

479 and therefore

$$\eta(x) = [G_0(x + d/2) + G_0(x - d/2)] \frac{\Pi w (h_0 - y_d)}{1 - \Pi w \beta_1}. \quad (75)$$

480 This is consistent with our assumption that the interface solution crosses the defects within
 481 the ramps for sufficiently small positive $h_0 - y_d$, when the denominator is positive, i.e.,

$$\Pi < \Pi_n^{(2)} = \frac{1}{w\beta_1} = \frac{1}{w\beta_0[\exp(-d/\ell_c) + 1]} = \frac{\Pi_n^{(1)}}{\exp(-d/\ell_c) + 1} \leq \Pi_n^{(1)}. \quad (76)$$

482 As for the single defect, this is the criterion for weakness of the pair of defects, and $\Pi_n^{(2)}$
483 is the (narrow-defect approximation of) the critical slope for the transition from weak to
484 strong. This method can be extended to an arbitrary number of defects which can also have
485 different defect strengths (disordered media). Note that this critical slope for the two-defect
486 system is always smaller than the one for the single defect, $\Pi_n^{(1)}$. This holds for defects of
487 arbitrary width; for derivation of the critical slope $\Pi_c^{(2)}$ for this case see Appendix A. For
488 slopes within $\Pi_c^{(2)} < \Pi < \Pi_c^{(1)}$, each defect is non-dissipative (weak) when isolated (single
489 defect only), whereas a system of two such defects is dissipative and hysteretic (strong).

Within the narrow-defect approximation, let us consider now a situation where the slope
of the individual defects is $\Pi < \Pi_n^{(1)}$, that is, each defect by itself is weak. The two-defect
system is strong if $\Pi > \Pi_n^{(2)}$, implying that

$$[\exp(-d/\ell_c) + 1] > \frac{\Pi_n^{(1)}}{\Pi}. \quad (77)$$

490 This inequality indicates that the two-defect system becomes strong if the separation dis-
491 tance d between the defect centers is $w \leq d < d_c$, where

$$d_c = \ell_c \ln \left(\frac{\Pi}{\Pi_n^{(1)} - \Pi} \right). \quad (78)$$

492 This is meaningful only for $d_c > w \approx 0$, that is, for $\frac{\Pi_n^{(1)}}{2} \leq \Pi < \Pi_n^{(1)}$. Thus, there is a factor
493 of two between the largest and smallest slopes where a single defect is weak but a pair can
494 be strong. The factor of two reduces for wider defects; in the limit $w/\ell_c \gg 1$, it approaches
495 unity, as the critical slope approaches $\rho g_e = \gamma/\ell_c^2$, independent of d .

496 Considering the case when the interface solution crosses the defects within the plateaus,
497 Eq. (25) (with a_1 replaced by a_2) gives for narrow defects

$$\eta(x) = \Pi w \ell_s [G_0(x + d/2) + G_0(x - d/2)]. \quad (79)$$

498 At the defects, this gives

$$\eta(\pm d/2) = \frac{\Pi w \ell_s \ell_c}{2\gamma} [1 + \exp(-d/\ell_c)] = \frac{\Pi}{\Pi_n^{(2)}} \ell_s, \quad (80)$$

499 a result analogous to the single-defect case [see Eq. 36]. For dissipation calculations, since
 500 the width of the defect cannot be neglected, we write

$$\eta(x) = \frac{\Pi}{\Pi_n^{(2)}} \ell_s \begin{cases} \exp\{-[|x| - (d+w)/2]/\ell_c\}, & |x| > (d+w)/2, \\ \cosh[x/\ell_c]/\cosh[(d-w)/(2\ell_c)], & |x| < (d-w)/2, \\ 1, & (d-w)/2 < |x| < (d+w)/2, \end{cases} \quad (81)$$

501 where we have assumed that $\eta(x)$ is constant within the defects, and equal to Eq. (80), and
 502 the first two lines are, essentially, Eq. (79), with d replaced by $d+w$ in the first line and
 503 $d-w$ in the second (a negligible change) to make the result continuous. If the pair is strong
 504 ($\Pi/\Pi_n^{(2)} > 1$), during imbibition the interface experiences a jump when it first touches the
 505 defects, just as in the single-defect case; thus, the interface configurations before and after
 506 the jump are

$$h_{\text{imb}}^- = y_d \quad (82)$$

507 and

$$h_{\text{imb}}^+ = y_d + \frac{\Pi}{\Pi_n^{(2)}} \ell_s \begin{cases} \exp\{-[|x| - (d+w)/2]/\ell_c\}, & |x| > (d+w)/2, \\ \cosh[x/\ell_c]/\cosh[(d-w)/(2\ell_c)], & |x| < (d-w)/2, \\ 1, & (d-w)/2 < |x| < (d+w)/2. \end{cases} \quad (83)$$

508 Likewise, during drainage the interface behaves similarly to the single-defect case, where the
 509 jump occurs when it reaches the boundary between the plateau and the ramp, with

$$h_{\text{dra}}^- = \begin{cases} y_d - \ell_s \left\{ \frac{\Pi}{\Pi_n^{(2)}} (1 - \exp\{-[|x| - \frac{d+w}{2}]/\ell_c\}) - 1 \right\}, & |x| > (d+w)/2, \\ y_d - \ell_s \left\{ \frac{\Pi}{\Pi_n^{(2)}} (1 - \cosh[\frac{x}{\ell_c}]/\cosh[\frac{d-w}{2\ell_c}]) - 1 \right\}, & |x| < (d-w)/2, \\ y_d + \ell_s, & (d-w)/2 < |x| < (d+w)/2 \end{cases} \quad (84)$$

510 and

$$h_{\text{dra}}^+ = y_d - \ell_s (\Pi/\Pi_n^{(2)} - 1). \quad (85)$$

511 The corresponding calculations of interface shapes for defects of an arbitrary width can be
 512 done numerically using the method in Appendix B.

513 The dissipated energy in imbibition and drainage can be evaluated using eqs. (50) and
 514 (52), with the values of h_{imb}^{\pm} and h_{dra}^{\pm} computed analytically or numerically, and the ex-
 515 pressions for the integrals of $F(x, y)$ from Eqs. (61)–(62), where $\text{Rect}(x/w)$ are replaced
 516 by $\text{Rect}([x + d/2]/w) + \text{Rect}([x - d/2]/w)$. For the narrow defect approximation, using
 517 Eqs. (82)–(85), as well as Eq. (76) for $\Pi_n^{(2)}$, the result reads

$$\Psi_{\text{imb}} = \Psi_{\text{dra}} = -w\ell_s^2\Pi \left[\frac{\Pi}{\Pi_n^{(2)}} - 1 \right]. \quad (86)$$

518 This expression resembles its counterpart for the single-defect case, Eq. (67), except for
 519 the critical threshold at which dissipation approaches zero [$\Pi_n^{(2)}$ instead of $\Pi_n^{(1)}$] and the
 520 factor of two; this is intuitive, as for two defects far apart the dissipation is additive, and the
 521 threshold remains the same. Equation (86) is also consistent with the fact that two touching
 522 defects ($d = w$) are equivalent to a single defect of twice the width. Finally, we find that
 523 the accuracy of the narrow-defect theory can be improved upon replacing in Eq. (86) the
 524 approximate threshold, $\Pi_n^{(2)}$, with the exact result, $\Pi_c^{(2)}$ [Eqs. (A3)–(A4)], providing

$$\Psi_{\text{imb}} = \Psi_{\text{dra}} = -w\ell_s^2\Pi \left[\frac{\Pi}{\Pi_c^{(2)}} - 1 \right]. \quad (87)$$

525 B. Interactions between a pair of weak defects: Numerical verification

526 To examine these intriguing theoretical predictions, we use numerical computations and
 527 simulations varying the distance d for a fixed defect shape (slope Π , ramp length ℓ_s , width
 528 w), computing the energy dissipated during the imbibition and drainage trajectories (see
 529 Appendix C for parameter values). We calculate the dissipated energy using (i) the numeri-
 530 cal computations described in Appendix B; (ii) direct numerical simulations of the interface
 531 evolution and the corresponding energy dissipation [12] (referred to as simulations, to dis-
 532 tinguish from the numerical computations of Appendix B). While the numerical simulations
 533 are more computational costly than the computations in Appendix B, the simulations can be
 534 used for any arbitrary capillary pressure field $p_c(x, y)$ (e.g. disorder with prescribed defect
 535 strength distributions in [12]).

536 Our numerical evaluations show that for pairs of weak defects sufficiently far apart, $d > d_c$
 537 [where d_c is approximated by Eq. (78)], there is no dissipation and hysteresis (Video S2 in

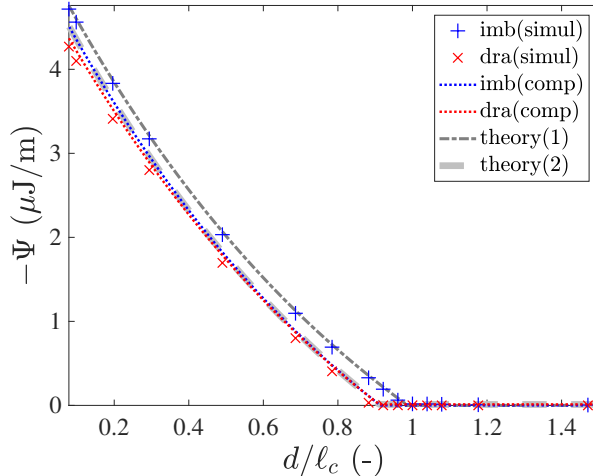


FIG. 6. Emergence of energy dissipation (“*strong*” behavior) in a pair of *weak* defects. As long as the defects are sufficiently far apart ($d > d_c$), the system is reversible and there is no dissipation. Once $d < d_c$, the displacement becomes irreversible, and dissipation and hysteresis emerge. We plot the dissipation calculated from simulations ([12]) and numerical computation (Appendix B; dotted lines), where blue and red refer to imbibition and drainage, respectively. Also plotted are the analytical solutions from two variants of the narrow defect theory: (1) Eq. (86) (approximate $\Pi_n^{(2)}$ [dash-dot]; and (2) the more accurate Eq. (87) with an exact value of $\Pi_c^{(2)}$ [thick dashed].

538 SI), whereas for $d < d_c$, dissipation emerges (Fig. 6). This dissipation arises from abrupt
 539 jumps of the interface along the defect slope in both imbibition and drainage, such that the
 540 PS response becomes hysteretic; the closer the defects are, the stronger the dissipation (and
 541 the width of the hysteresis cycle, e.g. see Videos S3–S4 in SI).

542 As expected for narrow defects, [Eq. (86)], the numerical computations give nearly identi-
 543 cal dissipated amounts for imbibition and drainage. The simulations provide similar results,
 544 though slightly exaggerate the difference between imbibition and drainage, due to numerical
 545 discretization errors (can be reduced by refinement, at the expense of higher computational
 546 cost). The distance at which dissipation vanishes in the numerical computations is identi-
 547 cal to the exact result for the critical distance from Eqs. (A3)–(A4) (“theory(2)” in legend
 548 of Fig. 6). The narrow defect theory [dissipation from Eq. (86) and critical distance from
 549 Eq. (78); “theory(1)” in legend of Fig. 6] provides a reasonable approximation. For wider
 550 defects, the deviation between the dissipation computed in imbibition and drainage, and
 551 between these and the dissipation evaluated with Eq. (87), increases. We note that the close
 552 agreement between the simulated dissipation for imbibition and Eq. (86) is coincidental.

553 C. Interactions between a pair of weak defects: Experimental observation

554 Here, we provide an experimental proof-of-concept showing the emergence of dissipation
555 in a pair of weak defects as they are brought close to each other. We use 3-D printing to
556 manufacture a series of systems (imperfect Hele-Shaw cells), with a single weak defect and
557 two pairs of identical defects at two different separation distances. As we cannot measure
558 the energy dissipated experimentally, we use the hysteresis cycle as a proxy for reversibility;
559 the larger the area within a closed PS cycle is, the larger the dissipation [12]. Details of
560 the experiments including the manufacturing, setup and image analysis, are provided in
561 Appendix D.

562 Our experiments validate the findings we obtained theoretically and numerically: while a
563 single regular defect of given geometry (weak) can behave reversibly, showing no hysteresis
564 (and thus no dissipation) (Fig. 7a; see also Video S5 in SI), a pair of defects (each of identical
565 geometry to the former) close enough together becomes hysteretic (Fig. 7b; Video S6 in SI)
566 due to the spatial interactions between the otherwise reversible entities. Decreasing the
567 pair separation increases the hysteresis (Fig. 7c; Video S7 in SI). In Fig. 7, we measure the
568 maximum deformation η_m along the middle line of the defect, and the baseline position h_f
569 as the vertical distance between the unperturbed interface (far from the defect) and the
570 bottom of the defect, i.e., $h_f = h_0 - y_d$ (see also Fig. 1).

571 We note that in these experiments, effects that are not considered in our 2-D linear
572 model can be of importance [31]. One such effect is large interface deformation resulting
573 in nonlinear curvature, where in our 2-D model we (i) approximate the total curvature as
574 the sum of in- and out-of-plane components, and (ii) use a linear approximation for the
575 former (vs. the full nonlinear formulation, e.g. see [23]). Further differences between our
576 2-D model and the experiments arise from 3-D effects related to (i) the curvature of the
577 meniscus between adjacent defects; (ii) the finite width of the meniscus in-plane projection;
578 and (iii) thin liquid film advancing ahead of the experimentally-observed *2-D projection* of
579 the (3-D) meniscus, resulting in an uncertainty in its position, hence $\eta_m > 0$ at $h_f < 0$
580 in Fig. 7; see further elaboration in Appendix D. These effects preclude a quantitative
581 comparison between our theoretical predictions and the experiments, which are presented
582 here as proof-of-concept that qualitatively supports our theory.

583 Interestingly, we expect the curvature of the meniscus between adjacent defects to lead

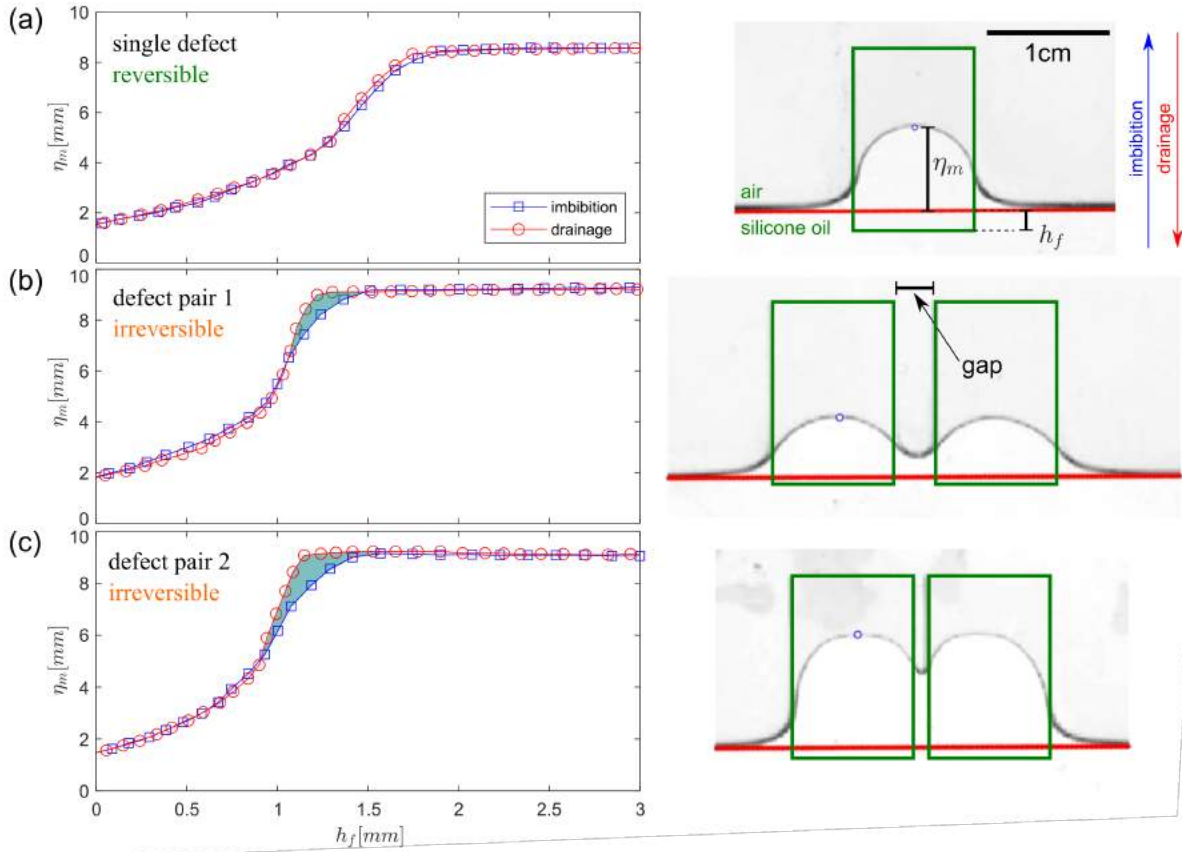


FIG. 7. Imbibition-drainage cycle for a single regular defect (a) and a pair of regular defects of width $w = 10$ mm, with a separation (measured between their centres) d of (b) 13 mm and (c) 11 mm, respectively. For each case, we show the imbibition-drainage trajectories in terms of the interface deformation η_m vs. its baseline position h_f (left panels) and an experimental image of the interface (right). Here η_m is the distance between the blue dot and the red line. Defects are highlighted by green rectangles. While the interface moves through a single regular defect reversibly, i.e. with no hysteresis and therefore no dissipation (a), a pair of such defects close enough together exhibits hysteresis (b), which increases as their separation distance decreases (c), confirming our theoretical prediction.

584 to a very different response of (i) two weak defects of width w in close proximity and (ii)
585 a single defect of width $2w$. This is because for a very narrow (yet finite) gap between the
586 defects ($d \approx w$), additional liquid-solid interfaces (of a finite area) are created. This change
587 in meniscus configuration is expected to affect the dissipation and hysteresis. In our 2-D
588 model, the amount of energy dissipated in these two cases will approach each other (cf.
589 Eq. (86)).

590 VI. CONCLUSIONS

591 In this paper, we study energy dissipation during quasi-static fluid-fluid displacements
592 across an imperfect Hele-Shaw cell (with “defects” i.e. local perturbations in thickness and
593 thus capillary pressure p_c). To explore the fundamental mechanisms for energy dissipation
594 and hysteresis, we consider a simple system comprising of isolated (single) defects of two
595 shapes: “regular” with *continuous* (here linear) variations in p_c (in the direction of fluid
596 advancement), and “mesa” defects where p_c changes *abruptly*. Depending on the slope of
597 p_c , the system can be classified as either (i) “weak”, where the interface passage across
598 the defect (imbibition and drainage) is fully reversible with no dissipation and hysteresis;
599 and (ii) “strong”, with dissipation and hysteresis. We derive analytical expressions for
600 the evolution of the fluid-fluid configuration as it deforms when it passes through defects
601 and the corresponding energy dissipation, which are validated numerically. The analysis
602 exposes subtle morphological differences between imbibition and drainage, originating from
603 the differences in wet area when a jump occurs.

604 A novel intriguing finding is that irreversible, hysteretic behavior and the associated
605 energy dissipation can emerge from the interaction of weak defects—objects which are in-
606 trinsically (when isolated) non-dissipative and non-hysteretic. This is demonstrated for a
607 simple system: a pair of identical weak defects, varying their separation distance. While far
608 enough apart, the pair of defects behaves as weak. Once the defect distance falls below a
609 threshold—dictated by surface tension and the system parameters (defect width and slope
610 of p_c), it becomes strong, producing hysteresis and dissipation. We compute this threshold
611 and the energy dissipated analytically, for the approximation of narrow defects (width much
612 smaller than the capillary length), and numerically (for arbitrary width) using two methods:
613 (i) numerical simulations of the sequence of equilibrium configurations and (ii) numerical
614 computation of the equilibrium conditions. A proof-of-concept experiment using 3-D printed
615 cells demonstrates the emergence of irreversible, hysteretic behavior due to the interaction
616 between non-hysteretic, reversible defects, validating our theoretical findings.

617 The cooperative mechanism exposed here is uniquely highlighted by our model. In con-
618 trast, classical models for hysteresis such as compartment models [26] rely on the existence of
619 a basic hysteretic unit (“hysteron”), and the overall hysteretic response is simply the sum of
620 the responses of these units. In the zero-temperature RFIM isolated spin flips are reversible

621 [16], and thus individual spins play a role equivalent to our weak defects. Similarly to the
622 present case, hysteresis and dissipation in the RFIM emerge from the collective response
623 of the system, in the form of spin-flip avalanches triggered by the local spin-spin interac-
624 tions. A crucial difference, however, is that spin-spin interactions in RFIM are present in the
625 whole system, and thus irreversible events can occur anywhere. In contrast, the interaction
626 between defects in our system is mediated by the two-phase interface, so that irreversible
627 jumps and dissipation are localized at the interface. Interestingly, the emergence of hystere-
628 sis as a collective response of a system of individually non-hysteretic agents with continuum
629 responses, interacting at each step through the memory of the predecessors, was applied to
630 explain irreversibility in climate events [32].

631 To the best of our knowledge, our model is the first to describe how hysteresis of pressure-
632 saturation curves during cyclic flows in disordered media emerges from the interactions
633 among defects, in a physical, non-phenomenological manner. Specifically in the context of
634 fluid displacement, both (i) the “ink bottle effect”—the canonical conceptual model for the
635 pore-scale mechanism underlying pressure-saturation hysteresis [3], as well as (ii) the “Lev-
636 ertt model”—a compartment model predicting macroscopic hysteresis [26], do not include
637 the key concept of spatial distance among the basic units (pores or defects). An oversimplifi-
638 cation of the interactions between basic model units is also inherent to the classical capillary
639 bundle model used in soil physics to predict the pressure-saturation relationship [33]. We
640 argue that the cooperative mechanism unveiled here is the dominant mechanism responsible
641 for hysteresis in multiphase fluid systems, noting that other mechanisms such as contact
642 angle hysteresis in surface wetting [34, 35], changes in interfacial connectivity (snap-off) and
643 fluid trapping [2] also contribute to hysteresis.

644 In conclusion, we present a detailed, rigorous investigation of the fundamental process
645 of energy dissipation between consecutive metastable configurations in the passage of an
646 interface through topographical defects. In the quasi-static limit considered here, viscous
647 dissipation due to finite velocity of the interface displacement is disregarded. The sim-
648 plicity of this conceptual model allows systematic theoretical examination of the origins of
649 energy dissipation and hysteresis. The insights gained here considering individual defects
650 are of immediate relevance to disordered media containing multiple interacting defects [12].
651 Interesting directions for further studies are the introduction of mechanisms that are not
652 considered in the current model system, to gain understanding of two-phase flow in more

653 complex disordered systems such as porous and fractured materials [8]. One is dynamic
654 effects associated with viscous dissipation in rate-driven systems and at high flow rates, con-
655 necting insights gained from detailed investigation of single isolated defects [23]. Another
656 is the nonlinear, 3-D effects that were evident even in the simple experiments presented
657 here. Finally, links between our novel modelling approach and the RFIM and other lattice
658 models open the way to gain fundamental understanding of how cooperative interactions
659 among non-hysteretic, non-dissipative entities could lead to the emergence of hysteresis and
660 dissipation in a wide variety of driven disordered systems [36–38].

661 **Appendix A: Evaluating the critical slope**

662 Here, we derive the critical pressure slope for a *pair* of identical defects, from which we
663 obtain the result for a single defect by putting the two defects next to each other (equivalent
664 to a single defect of twice the width), or infinitely far apart (equivalent to a single defect of
665 the same width). To analyze defects of an arbitrary width, we use the original differential
666 equation for the interface shape, Eq. (1), instead of the Green’s function-based approach.

667 Consider a pair of defects of width w , with distance d between their symmetry axes, as
668 introduced in Section V. The capillary pressure profile is given by Eqs. (71), (72) and (23).
669 For the interface profile with $h_0 = y_d$, if the interface solution crosses the defects entirely
670 within the ramp regions, the equation for $\eta(x) = h(x) - y_d$ is

$$\gamma\eta'' = \begin{cases} (\rho g_e - \Pi)\eta, & ||x| - d/2| < w/2 \text{ (inside the defects),} \\ \rho g_e \eta, & ||x| - d/2| > w/2 \text{ (outside the defects).} \end{cases} \quad (\text{A1})$$

671 For $\Pi > \rho g_e$ the solutions are given by

$$\eta(x) = \begin{cases} C_1 \cosh(x/\ell_c), & |x| < (d - w)/2, \\ C_2 \cos[\sqrt{\Pi/\gamma - 1/\ell_c^2}x] + C_3 \sin[\sqrt{\Pi/\gamma - 1/\ell_c^2}x], & (d - w)/2 < |x| < (d + w)/2, \\ C_4 \exp(-|x|/\ell_c), & |x| > (d + w)/2. \end{cases} \quad (\text{A2})$$

672 The top line in (A2) corresponds to the space between the defects, the middle to the part of
673 the interface inside the defects, and the bottom to the outer regions. Matching conditions,

674 requiring that the values of $\eta(x)$ and its first derivative $\eta'(x)$ match at $|x| = (d - w)/2$ and
675 $|x| = (d + w)/2$, provide a system of four linear homogeneous equations for four unknowns
676 C_1 – C_4 , which has nontrivial solutions when its determinant is zero. Given the parameters
677 w , d , ℓ_c and γ , this can only be satisfied for a single value of $\Pi = \Pi_c^{(2)}$. For this value, a
678 continuum of nontrivial solutions exist, differing by the value of the prefactor from zero to
679 the maximum value for which the solution still crosses the defects entirely within the ramps.

680 The interpretation of this result is as follows. (i) For $\Pi < \Pi_c^{(2)}$, only the trivial solution
681 $\eta(x) = 0$ of the original equation (1) with $h_0 = y_d$ exists; as h_0 increases, this solution evolves
682 continuously, thus, the defect is weak. (ii) As Π increases, the rate of deformation, $d\eta_m/dh_0$
683 grows, approaching infinity as $\Pi \rightarrow \Pi_c^{(2)}$ from below, so that at $\Pi = \Pi_c^{(2)}$ an infinitesimal
684 change in h_0 gives rise to a finite deformation. This is consistent with the existence of a
685 continuum of solutions with $h_0 = y_d$ at $\Pi = \Pi_c^{(2)}$. (iii) for $\Pi > \Pi_c^{(2)}$ there are no nontrivial
686 solutions that cross the defects within the ramps, but there is one at least partially within
687 the plateaus and thus a jump occurs at $h_0 = y_d$ and the defect is strong. Then $\Pi_c^{(2)}$ is the
688 critical value separating weak and strong defect pairs.

689 By equating the determinant of the above-mentioned system of four equations to zero,
690 an equation for $\Pi_c^{(2)}$ can be obtained. We define a quantity ζ such that

$$\Pi_c^{(2)} = \gamma[1/\ell_c^2 + (\zeta/w)^2]. \quad (\text{A3})$$

691 Then, the following equation

$$\tan \zeta = \frac{1 + \tanh[(d - w)/(2\ell_c)]}{(\ell_c \zeta/w)^2 - \tanh[(d - w)/(2\ell_c)]} \frac{\ell_c \zeta}{w} \quad (\text{A4})$$

692 has one solution in the interval $0 < \zeta < \pi$, which, generally, needs to be found numerically,
693 and then $\Pi_c^{(2)}$ is given by Eq. (A3). If Π , w , ℓ_c and γ are given, a fully analytical solution
694 for the critical value of the distance d is possible.

695 Next, we verify that for narrow defects ($w/\ell_c \ll 1$), the result of Eq. (76) is recovered.
696 Assuming (to be confirmed by the calculation) that $w/\ell_c \ll \zeta \ll 1$, we can approximate
697 Eq. (A4) as

$$\zeta = \{1 + \tanh[d/(2\ell_c)]\} \frac{w}{\ell_c \zeta}, \quad (\text{A5})$$

698 the solution of which is

$$\zeta = \left[\frac{w}{\ell_c} \left(1 + \tanh \frac{d}{2\ell_c} \right) \right]^{1/2}. \quad (\text{A6})$$

699 This indeed satisfies the above inequality for ζ . Then, we write Eq. (A3),

$$\Pi_c^{(2)} = \gamma \left[\frac{1}{\ell_c^2} + \frac{1 + \tanh(d/2\ell_c)}{w\ell_c} \right] \approx \frac{\gamma[1 + \tanh(d/2\ell_c)]}{w\ell_c}, \quad (\text{A7})$$

700 which, after a simple transformation, coincides with Eq. (76). On the other hand, for $w \gg \ell_c$,
701 since ζ is finite, Eq. (A3) gives $\Pi_c^{(2)} = \gamma/\ell_c^2$ for any d .

702 Finally, we obtain the critical slope for a single defect by noting that for $d = w$ (two
703 defects put together with no gap), we get

$$\tan \zeta = \frac{w}{\ell_c \zeta}. \quad (\text{A8})$$

704 This corresponds to a single defect of width $2w$; then, for a single defect of width w ,

$$\tan u = \frac{w}{2\ell_c u}, \quad (\text{A9})$$

705 and

$$\Pi_c^{(1)} = \gamma[1/\ell_c^2 + (2u/w)^2]. \quad (\text{A10})$$

706 Equation (A9) is a transcendental equation for u that needs to be solved numerically. How-
707 ever, a fully analytic solution is possible for the critical value of w given Π , ℓ_c and γ . We
708 can also check that for two defects very far apart ($d - w \gg \ell_c$) this single-defect result is
709 recovered. Indeed, in this case Eq. (A4) becomes

$$\tan \zeta = \frac{2\ell_c \zeta/w}{(\ell_c \zeta/w)^2 - 1} = \frac{2(w/\ell_c \zeta)}{1 - (w/\ell_c \zeta)^2}. \quad (\text{A11})$$

710 Using the trigonometric identity $\tan 2X = 2 \tan X/(1 - \tan^2 X)$, we get

$$\tan(\zeta/2) = \frac{w}{\ell_c \zeta}, \quad (\text{A12})$$

711 which coincides with Eq. (A9) if $u = \zeta/2$; Eq. (A10) then coincides with Eq. (A3).

712 **Appendix B: Mixed numerical-analytical computation of the interface profile**

713 Here, we describe the mixed numerical-analytical method we have used to calculate the
 714 interface configuration $h(x)$, in particular, (i) after the jump during imbibition and (ii) before
 715 the jump during drainage. As similar approaches have been used for a single and a pair of
 716 defects, we describe both cases at the same time, indicating differences where applicable.

717 We consider capillary pressure profiles given by Eqs. (21)–(23) for a single defect, and
 718 Eqs. (71), (72), (23) for a pair. Thus, the defect consists of a ramp (slope) of length ℓ_s ,
 719 followed by a plateau. We only consider cases where in the range(s) of x where the defect(s)
 720 is (are) located, the interface is entirely within the defect(s), i.e. for $|x| < w/2$ (single
 721 defect) or $||x| - d/2| < w/2$ (pair), $y_d < h(x) < y_d + \ell$. The interface then obeys the
 722 following equation for a single defect,

$$\gamma h'' = \begin{cases} \rho g_e (h - h_0), & |x| > w/2, \\ \rho g_e (h - h_0) - \Pi(h - y_d), & |x| < w/2 \text{ and } h < y_d + \ell_s, \\ \rho g_e (h - h_0) - \Pi(\ell_s - y_d), & |x| < w/2 \text{ and } h > y_d + \ell_s \end{cases} \quad (\text{B1})$$

723 and for a defect pair,

$$\gamma h'' = \begin{cases} \rho g_e (h - h_0), & |x| > (d + w)/2, |x| < (d - w)/2 \\ \rho g_e (h - h_0) - \Pi(h - y_d), & ||x| - d/2| < w/2 \text{ and } h < y_d + \ell_s, \\ \rho g_e (h - h_0) - \Pi(\ell_s - y_d), & ||x| - d/2| < w/2 \text{ and } h > y_d + \ell_s. \end{cases} \quad (\text{B2})$$

724 In the outer region ($|x| > w/2$ for a single defect and $|x| > (d + w)/2$ for a pair), the
 725 solution is

$$h = h_0 + \eta_b \exp(-\Delta x / \ell_c), \quad (\text{B3})$$

726 where $\Delta x = |x| - w/2$ for a single defect or $\Delta x = |x| - (d + w)/2$ for a pair. The constant
 727 η_b , the value of h at the (outer) boundary of the defect, needs to be found based on the
 728 requirement that the solution is symmetric, thus, $h'(0) = 0$, by matching to other parts of
 729 the solution, as discussed below; the solution for η_b may or may not exist depending on h_0
 730 and the parameters of the defect(s).

731 Inside the defect(s) ($|x| < w/2$ for a single defect or $||x| - d/2| < w/2$ for a pair), the

732 solution, in general, consists of pieces of functions that can be found analytically. As the
733 matching between these pieces is cumbersome, that part of the solution is obtained here
734 by numerical integration. Assuming that h_0 and η_b are known, the values of h and its first
735 derivative are provided from the outer solution at the $x = w/2$ [or $x = (d + w)/2$] boundary
736 of the defect, and can serve as the initial conditions for numerical integration. For a single
737 defect, integration can be carried out down to $x = 0$ to find out if the $h'(0) = 0$ condition
738 is satisfied. Thus, we can find η_b by solving the $h'(0) = 0$ equation using the bisection
739 root-finding scheme [39, Chapter 9.1]. For a pair of defects, $x = 0$ is in the middle between
740 the defects; in that region between the defects, the analytical solution with $h'(0) = 0$ is

$$h(x) = h_0 + C \cosh(x/\ell_c), \quad (\text{B4})$$

741 where C is an unknown constant. This gives the condition on the values of h and its first
742 derivative on the inner boundary of the defect,

$$\frac{h'([d - w]/2)}{h([d - w]/2) - h_0} = \frac{1}{\ell_c} \tanh \frac{d - w}{2\ell_c}. \quad (\text{B5})$$

743 By integrating numerically down to $(d - w)/2$ within the defect, we find if this condition
744 is satisfied, which, as before provides an equation for the bisection scheme to find η_b . We
745 note that for $\Pi > \rho g_e$ the solution for $|x| < w/2$ (or $||x| - d/2| < w/2$) can be oscillatory
746 and it is possible that several roots η_b and associated solutions exist. However, apart from
747 the solution with a single maximum inside (each) defect, these solutions go below y_d and as
748 such violate the conditions outlined above.

749 During imbibition, the interface jump happens once the interface touches the defect.
750 Thus, $h_{\text{imb}}^- = y_d$ and h_{imb}^+ is the solution of Eq. (B1) or (B2) with $h_0 = y_d$. This solution can
751 be found as described above. For drainage, the situation is more complicated, because h_0 is
752 unknown. Its value is a bifurcation point such that for lower values there are no solutions
753 crossing the defect. In other words, for lower h_0 , regardless of the value of η_b , the defect
754 will not sufficiently deform the interface. For a single defect this means that the maximum
755 possible value of $h'(0)$ is below zero; for a pair, the maximum possible value of the ratio on
756 the left-hand side of Eq. (B5) is smaller than its right-hand side. We then carry out a nested
757 procedure, where in the inner cycle, for a particular h_0 we find the maximum value of $h'(0)$

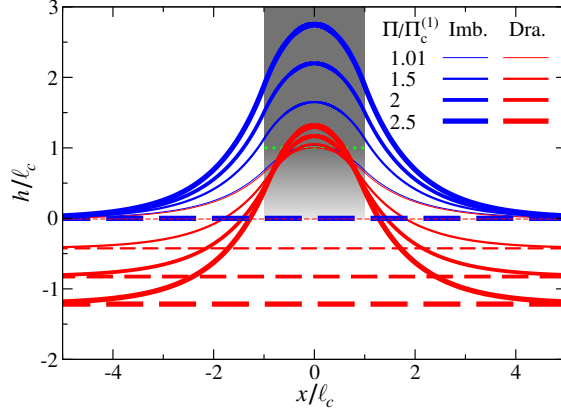


FIG. 8. Interface profiles before and after jumps for an intermediate-width ($w/\ell_c = 2$) regular defect, for different capillary pressure slopes. The ramp part of the defect is shown as gradient shading and the plateau part in uniform gray. The boundary between these two regions at $h/\ell_c = 1$ is marked with a green dotted line. Dashed and solid lines represent the undeformed (flat) and deformed configurations, i.e. before and after the jump in imbibition, and the opposite in drainage. These results are complementary to those shown in Fig. 3.

758 (for a single defect) or of the left-hand side of Eq. (B5) (for a pair), using the golden-section
 759 algorithm [39, Chapter 10.2], and then, via bisection, find the value of h_0 for which this
 760 maximum value is zero (for a single defect) or the right-hand side of Eq. (B5) (for a pair).
 761 This eventually provides both h_{dra}^- and h_{dra}^+ (the latter equal to the value of h_0 resulting
 762 from the procedure).

763 The above procedure was used to find the interface shapes for narrow and wide single
 764 defects in Fig. 3. For clarity, we add a similar plot for the general case of a defect of an
 765 intermediate width ($w/\ell_c = 2$; Fig. 8). Overall, qualitatively, the results are intermediate
 766 between the limits of wide and narrow defects. However, notably, for imbibition, while in
 767 both limits $\eta(0)/\ell_s = \Pi/\Pi_c^{(1)}$, here the value of $\eta(0)$ is slightly higher, thus, the dependence
 768 of $\eta(0)$ on the defect width is non-monotonic.

769 Once the interface profiles before and after the jump are found, the dissipated energy
 770 can be calculated using Eqs. (50) and (52), where the integration is carried out numerically
 771 inside the defect(s) and analytically outside. Note that if one fixes η_b (for imbibition) or
 772 h_0 (for drainage), the corresponding value of d for which Eq. (B5) is satisfied can be found
 773 directly, avoiding bisection. This can be used to speed up computations when obtaining Ψ
 774 vs d data (Fig. 6), by varying η_b (or h_0) and producing a table of $[\Psi, d]$ values.

775 **Appendix C: Numerical details**

776 For the results shown in Fig. 6 (and Videos S2–S4 in SI), we use the following parameters:
 777 $g_e = 0.2 \text{ m/s}^2$, $\rho = 998 \text{ kg/m}^3$, $\gamma = 20.7 \text{ mN/m}$ (such that $\ell_c \approx 10.2 \text{ mm}$). The defect width
 778 is $w = 0.8 \text{ mm}$, which means that it is relatively narrow ($w/\ell_c \approx 0.08$), and we expect the
 779 narrow defect theory to yield a good approximation. The defect profile is such that δp_c
 780 changes linearly between zero and $\approx 7.39 \text{ Pa}$ along a slope of length $\ell_s = 2 \text{ mm}$. For these
 781 values, an isolated single defect is weak, as the pressure slope, $\Pi \approx 3.70 \times 10^3 \text{ Pa/m}$, is
 782 smaller than the critical value for a single defect, computed using both (i) the narrow-defect
 783 approximation, with Eq. (34) giving $\Pi_n^{(1)} \approx 5.08 \times 10^3 \text{ Pa/m}$; and (ii) the exact arbitrary-
 784 width result of Appendix A, with Eqs. (A9)–(A10), such that $\Pi_c^{(1)} \approx 5.22 \times 10^3 \text{ Pa/m}$.

785 **Appendix D: Experimental details**

786 An imperfect Hele-Shaw cell was manufactured using stereolithography 3-D printing. The
 787 cell was produced with three sets of defects: a single defect and two sets of defect pairs with
 788 varying inter-defect gaps, see Fig. 9 (a). This efficient design allows us to run three separate
 789 experiments on the same cell in sequence.

791 To experimentally produce variations in the capillary pressure δp_c , we introduce modula-
 792 tions of the Hele-Shaw cell gap space $b(x, y) = b_0 - \delta b(x, y)$. This introduces a local variation
 793 of the out-of-plane capillary pressure $p_c(x, y) = p_c^0 + \delta p_c(x, y)$, where $p_c^0 = 2\gamma \cos(\theta)/b_0$ (θ
 794 being the contact angle) and $\delta p_c = p_c^0 \delta b / (b_0 - \delta b)$ [15]. We design the functional form of
 795 $\delta b(y)$ such that the the capillary pressure $p_c(x, y)$ within the defect is a linear function of y ,
 796 i.e., $\delta p_c(x, y) = \Pi(y - y_d)$ for $y_d < y \leq y_d + \ell_s$, and $\delta p_c(x, y) = \Pi \ell_s$ for $y_d + \ell_s < y < y_d + \ell$.
 797 The length of the sloping part of the defect is $\ell_s = 10 \text{ mm}$ and $\ell_p = \ell - \ell_s = 5 \text{ mm}$ is
 798 the length of the constant capillary pressure zone (plateau) after the slope. The defect
 799 width is $w = 10 \text{ mm}$. The value for the pressure slope $\Pi = dp_c/dy$ was chosen through a
 800 series of experiments as $\Pi = 6 \times 10^3 \text{ Pa/m}$. This value was chosen as it provides interface
 801 deformations that are large enough to be easily captured by image analysis, while not too
 802 large to avoid highly nonlinear deformations and snap-off events during drainage. Under
 803 these conditions, the defect profile is: $\delta b(y) = b_0 - \left(\frac{\Pi(y - y_d)}{2\gamma} + \frac{1}{b_0} \right)^{-1}$ for $y_d < y \leq y_d + \ell_s$,
 804 and $\delta b(y) = \delta b(\ell_s)$ for $y_d + \ell_s < y < y_d + \ell_s + \ell_p$ (here we made the assumption that the

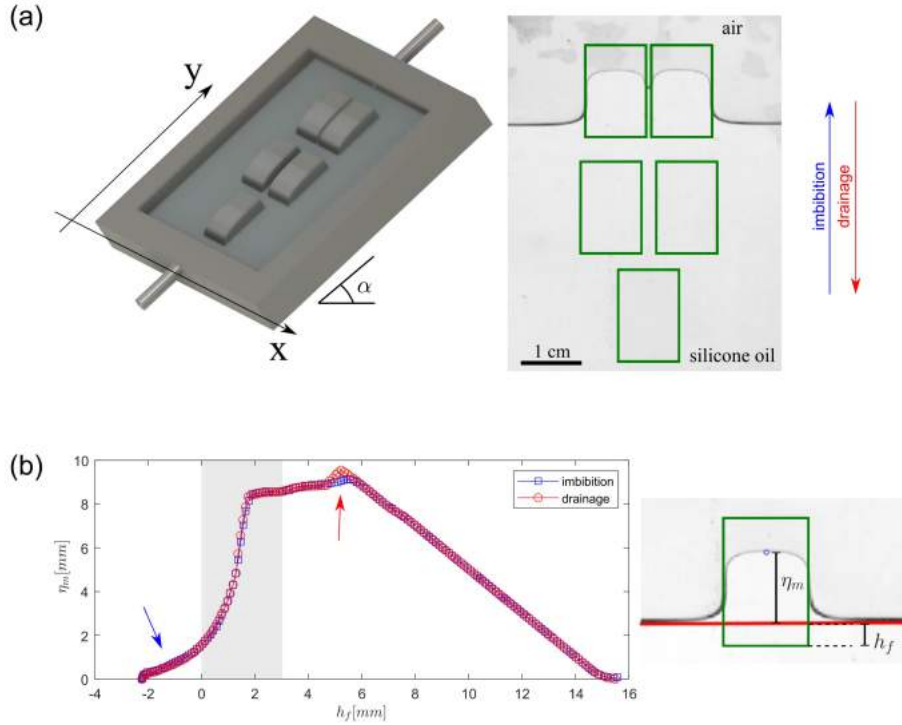


FIG. 9. (a) A 3-D printed including the 3 sets of defects (left), with a typical image of the interface during an experiment (right), showing the interface deformation due to its interaction with the top defects (dark green rectangles). Silicone oil enters from the bottom to displace the air initially filling the cell. The oil-air interface advances (imbibition) and recedes (drainage) in response to an increase or decrease in the oil pressure at the bottom of the cell, respectively. The cell is tilted by an angle $\alpha = 38^\circ$ with respect to the horizontal. (b) Imbibition-drainage cycle for the single defect. For each frame analyzed, we track the unperturbed position of the interface far from the defect h_f and the maximum perturbation η_m of the interface with regards to the unperturbed position. The presented cycle is reversible, namely the defect is *weak*. In panel (b), the gray shaded area corresponds to the data shown in Fig. 7 (a), where the arrows point to interesting physical effects not considered in our theoretical analysis (see text).

805 liquid perfectly wets the medium, $\theta \approx 0^\circ$). The cell's area is $6 \text{ cm} \times 6 \text{ cm}$, with a depth
 806 of $b_0 = 3.6 \text{ mm}$. The non-wetting fluid is ambient air at atmospheric pressure. For wetting
 807 fluid we used silicone oil, with kinematic viscosity $\nu = 10 \text{ cSt} = 10 \text{ mm}^2/\text{s}$, surface tension
 808 against air $\gamma = 20 \text{ mN/m}$ and density $\rho = 0.93 \text{ g/mL}$. Silicone oils are highly wetting;
 809 to ensure nearly-perfect wetting conditions (a contact angle $\theta \approx 0$), we pre-wet all solid
 810 surfaces of the model with the same silicone oil used in the experiment. This is obtained
 811 by doing an imbibition-drainage cycle in the cell prior to the actual experiment; as the air
 812 drains the oil, it leaves a thin film of oil on the solid surfaces.

813 The experiment is driven by changing the height of a reservoir of silicone oil connected

814 to the inlet (bottom) of the model. As the reservoir height increases by δh , the oil pressure
815 at the bottom of the model increases by $\delta p = \rho g \sin(\alpha)\delta h$ thus causing the interface to move
816 upwards (imbibe), and vice versa in drainage. A moving average filter is applied to the h_f
817 and η_m data (in Figs. 7 and 9) to remove spurious high-frequency noise (a consequence of
818 image analysis inaccuracies).

819 The experiments in Fig. 7 *qualitatively* demonstrate that (1) the imbibition-drainage cy-
820 cle around a single defect can be reversible, thus characterizing a weak defect, and (2) the
821 interaction between weak defects can trigger irreversibility (hysteresis). The experiments
822 also reveal further intriguing physics not considered in our model. This is evident in the
823 reversible case shown in Fig. 9b: Examining the entire curve in Fig. 9b, outside the gray
824 shaded area which corresponds to the region in Fig. 7 where potential hysteresis and dis-
825 sipation may occur according to our model (see Fig. 2), exposes other interesting features.
826 The blue arrow in Fig. 9b points to a perturbation in the curve even before the baseline
827 position reaches the defect. This can be explained through the 3-D nature of the liquid-air
828 interface. As the silicone oil wets both the top and bottom surfaces of the cell, there is a
829 thin film of liquid ahead of the 2-D projected interface. Once this film touches the defect,
830 the perturbation starts to grow even before its 2-D projection touches the defect. Similarly,
831 the red arrow in Fig. 9b points to a small bump in the drainage cycle, which might be caused
832 by pinning of the contact line as it touches the defect in drainage. These 3-D effects are not
833 included in our 2-D model. The plateau region included after the sloping part of the defect
834 ensures that artifacts such as those related to contact line pinning (red arrow in Fig. 9b)
835 occur far from the area of interest in our model (gray shading in Fig. 9b).

836 ACKNOWLEDGMENTS

837 RH acknowledges support from the Engineering and Physical Sciences Research Council
838 (EP/V050613/1); MD, JO, and RP acknowledge the support of the Agencia Estatal de
839 Investigación (10.13039/501100011033), Ministerio de Ciencia e Innovación and European
840 Regional Development Fund “A way of making Europe” through grants HydroPore PID2019-
841 106887GB-C31 and C32, (MD and JO, respectively), PID2022- 839 137652NB-C41 and
842 C42 (MD and JO, respectively), and PID2021-122369NB-I00 (RP). MM acknowledges the

843 support from the Research Council of Norway through projects 262644 and 324555.

- 844 [1] M. Sahimi, *Flow and Transport in Porous Media and Fractured Rock* (Wiley VCH Verlag
845 GmbH, N.Y., 2011).
- 846 [2] B. Albers, Modeling the hysteretic behavior of the capillary pressure in partially saturated
847 porous media: A review, *Acta Mech.* **225**, 2163 (2014).
- 848 [3] W. B. Haines, Studies in the physical properties of soil. V. The hysteresis effect in capillary
849 properties, and the modes of moisture distribution associated therewith, *J. Agr. Sci.* **20**, 97
850 (1930).
- 851 [4] N. Morrow, Physics and thermodynamics of capillary action in porous media, *Ind. Eng. Chem.*
852 *Res.* **62**, 32 (1970).
- 853 [5] S. Berg, H. Ott, S. A. Klapp, A. Schwing, R. Neiteler, N. Brussee, A. Makurat, L. Leu,
854 F. Enzmann, J.-O. Schwarz, M. Kersten, S. Irvine, and M. Stampanoni, Real-time 3D imaging
855 of Haines jumps in porous media flow, *P. Natl. Acad. Sci. USA* **110**, 3755 (2013).
- 856 [6] L. Cueto-Felgueroso and R. Juanes, A discrete-domain description of multiphase flow in porous
857 media: Rugged energy landscapes and the origin of hysteresis, *Geophys. Res. Lett.* **43**, 1615
858 (2016).
- 859 [7] J. O. Helland, E. Jettestuen, and H. A. Friis, A discrete-domain approach to three-phase
860 hysteresis in porous media, *Water Resour. Res.* **57**, e2021WR029560 (2021).
- 861 [8] K. J. Måløy, M. Moura, A. Hansen, E. G. Flekkøy, and R. Toussaint, Burst dy-
862 namics, up-scaling and dissipation of slow drainage in porous media, *Front. Phys.* **9**,
863 10.3389/fphy.2021.796019 (2021).
- 864 [9] J. E. McClure, S. Berg, and R. T. Armstrong, Thermodynamics of fluctuations based on
865 time-and-space averages, *Phys. Rev. E* **104**, 035106 (2021).
- 866 [10] B. K. Primkulov, J. Y. Y. Chui, A. A. Pahlavan, C. W. MacMinn, and R. Juanes, Character-
867 izing dissipation in fluid-fluid displacement using constant-rate spontaneous imbibition, *Phys.*
868 *Rev. Lett.* **125**, 174503 (2020).
- 869 [11] D. Bedeaux and S. Kjelstrup, Fluctuation-dissipation theorems for multiphase flow in porous
870 media, *Entropy* **24** (2022).
- 871 [12] R. Holtzman, M. Dentz, R. Planet, and J. Ortín, The relation between dissipation and

- 872 memory in two-fluid displacements in disordered media, *Geophysical Research Letters* **50**,
873 e2023GL104073 (2023).
- 874 [13] J. F. Joanny and P.-G. de Gennes, A model for contact angle hysteresis, *J. Chem. Phys.* **81**,
875 552 (1984).
- 876 [14] R. Planet, L. Díaz-Piola, and J. Ortín, Capillary jumps of fluid-fluid fronts across an elemen-
877 tary constriction in a model open fracture, *Phys. Rev. Fluids* **5**, 044002 (2020).
- 878 [15] R. Holtzman, M. Dentz, R. Planet, and J. Ortín, The origin of hysteresis and memory of
879 two-phase flow in disordered media, *Commun. Phys.* **3**, 222 (2020).
- 880 [16] J. P. Sethna, K. Dahmen, S. Kartha, J. A. Krumhansl, B. W. Roberts, and J. D. Shore,
881 Hysteresis and hierarchies: Dynamics of disorder-driven first-order phase transformations,
882 *Phys. Rev. Lett.* **70**, 3347 (1993).
- 883 [17] J. Ortín and J. Goicoechea, Dissipation in quasistatically driven disordered systems, *Phys.*
884 *Rev. B* **58**, 5628 (1998).
- 885 [18] P.-G. de Gennes, Imperfect Hele-Shaw cells, *J. Physique (Paris)* **47**, 1541 (1986).
- 886 [19] J. Soriano, J. Ramasco, M. Rodríguez, A. Hernández-Machado, and J. Ortín, Anomalous
887 roughening of Hele-Shaw flows with quenched disorder, *Phys. Rev. Lett.* **89**, 026102 (2002).
- 888 [20] D. Geromichalos, F. Mugele, and S. Herminghaus, Nonlocal dynamics of spontaneous imbibi-
889 tion fronts, *Phys. Rev. Lett.* **89**, 104503 (2002).
- 890 [21] H. Darcy, *Les fontaines publiques de la ville de Dijon*. (Victor Dalmont, Paris, 1856).
- 891 [22] P. G. Saffman and G. Taylor, The penetration of a fluid into a porous medium or Hele-Shaw
892 cell containing a more viscous liquid, *Proc. R. Soc. A* **245**, 312 (1958).
- 893 [23] I. Lavi, L. Rose, R. Planet, J. Casademunt, S. Santucci, and J. Ortín, Prebifurcation enhance-
894 ment of imbibition-drainage hysteresis cycles, *Phys. Rev. Fluids* **8**, 124002 (2023).
- 895 [24] J. P. Sethna, K. A. Dahmen, and O. Perkovic, Chapter 2 – random-field ising models of
896 hysteresis, in *The Science of Hysteresis*, edited by G. Bertotti and I. D. Mayergoyz (Academic
897 Press, 2006) pp. 107 – 179.
- 898 [25] A. A. Middleton, Asymptotic uniqueness of the sliding state for charge-density waves, *Physical*
899 *Review Letters* **68**, 670 (1992).
- 900 [26] G. Bertotti and I. D. Mayergoyz, eds., *The Science of Hysteresis* (Academic Press, 2006).
- 901 [27] J. Goicoechea and J. Ortín, Hysteresis and return-point memory in deterministic cellular
902 automata, *Phys. Rev. Lett.* **72**, 2203 (1994).

- 903 [28] N. C. Keim, J. D. Paulsen, Z. Zeravcic, S. Sastry, and S. R. Nagel, Memory formation in
904 matter, *Rev. Mod. Phys.* **91**, 035002 (2019).
- 905 [29] H. Bense and M. van Hecke, Complex pathways and memory in compressed corrugated sheets,
906 *Proc. Nat. Acad. Sci. USA* **118**, 10.1073/pnas.2111436118 (2021).
- 907 [30] L. Díaz-Piola, R. Planet, O. Campàs, J. Casademunt, and J. Ortín, Fluid front morphologies
908 in gap-modulated hele-shaw cells, *Phys. Rev. Fluids* **2**, 094006 (2017).
- 909 [31] We also note that our 2-D model is strictly valid only when the out-of-plane thickness varies
910 slowly in space, while in the examples considered here the defects contain abrupt changes in
911 thickness.
- 912 [32] M. Lim and C. Saloma, Emergence of hysteresis in a network of nonhysteretic agents with
913 continuous responses, *Phys. Rev. Lett.* **88**, 038701 (2002).
- 914 [33] A. G. Hunt, R. P. Ewing, and R. Horton, What’s wrong with soil physics?, *Soil Sci. Soc. Am.*
915 *J.* **77**, 1877 (2013).
- 916 [34] M. O. Robbins and J. F. Joanny, Contact angle hysteresis on random surfaces, *EPL-Europhys.*
917 *Lett.* **3**, 729 (1987).
- 918 [35] A. Giacomello, L. Schimmele, and S. Dietrich, Wetting hysteresis induced by nanodefects,
919 *Proc. Nat. Acad. Sci. USA* **113**, E262 (2016).
- 920 [36] C. W. Lindeman and S. R. Nagel, Multiple memory formation in glassy landscapes, *Sci. Adv.*
921 **7**, eabg7133 (2021).
- 922 [37] K. J. Wiese, Theory and experiments for disordered elastic manifolds, depinning, avalanches,
923 and sandpiles, *Rep. Prog. Phys.* **85**, 086502 (2022).
- 924 [38] D. Shohat and Y. Lahini, Dissipation indicates memory formation in driven disordered sys-
925 tems, *Phys. Rev. Lett.* **130**, 048202 (2023).
- 926 [39] W. H. Press, S. A. Teukolsky, W. T. Vetterling, and B. P. Flannery, *Numerical Recipes*, 3rd
927 ed. (Cambridge University Press, Cambridge, UK, 2007).